Real-time monitoring of static elastic modulus evolution in hardening concrete through longitudinal-wave velocity changes retrieved by the stretching technique

Cheng, Hao; Liang, Minfei

DOI
10.1016/j.conbuildmat.2024.139086

Publication date
2024

Document Version
Final published version

Published in
Construction and Building Materials

Construction and Building Materials 453 (2024) 139086

Contents lists available at ScienceDirect

Construction and Building Materials

journal homepage: www.elsevier.com/locate/conbuildmat

Real-time monitoring of static elastic modulus evolution in hardening concrete through longitudinal-wave velocity changes retrieved by the stretching technique

Hao Cheng [a], Minfei Liang [b,c,*]

[a] Department of Engineering Structures, Faculty of Civil Engineering and Geosciences, Delft University of Technology, Stevinweg 1, Delft 2628 CN, the Netherlands
[b] Department of Materials, Mechanics, Management & Design, Faculty of Civil Engineering and Geosciences, Delft University of Technology, Stevinweg 1, Delft 2628 CN, the Netherlands
[c] Clarendon Laboratory, Department of Physics, University of Oxford, Oxford, Great Britain OX1 3PU, UK

ARTICLE INFO

Keywords:
Concrete hydration
Direct wave interferometry
Static and dynamic elastic modulus
The stretching technique
Ultrasonics

ABSTRACT

Monitoring of gradual increase in elastic modulus of concrete over time is crucial for designing structures exposed to early age loading and predicting long-term deformations, such as creep. Two primary methods are used to assess elastic modulus: the static method, involving compression tests, and the dynamic method, utilizing approaches like EMM-ARM (E-modulus Measurement through Ambient Response Method), impact-echo, and ultrasonic approach. The static method, although destructive, yields the static or secant modulus, directly applicable for structural design. However, it cannot be utilized to track changes in elastic modulus within the existing structure caused by factors such as hydration, freeze-thaw, or chemical attack. In contrast, the non-destructive dynamic method can monitor these changes in the existing structure. Yet, the elastic modulus obtained through this method, known as the dynamic elastic modulus, represents the initial tangent modulus and is generally higher than the static modulus. To estimate the static elastic modulus through the non-destructive ultrasonic approach, we propose a new signal processing technique using direct wave interferometry (DWI) in this study. To validate the elastic modulus estimated through this technique, embeddable ultrasonic sensors are installed in the specimen within the temperature stress testing machine (TSTM). The experimental results show that the elastic modulus derived from the newly proposed DWI-based ultrasonic approach consistently provides more accurate estimates of the static elastic modulus compared to the UPV-based dynamic elastic modulus. The relative errors between the DWI-based and compression test-based elastic moduli on 7-day is 2.6 %. This approach also enables the tracking of static elastic modulus changes due to freeze-thaw cycles or chemical attacks.

1. Introduction

Concrete, the most commonly used construction material worldwide, undergoes a gradual evolution of mechanical properties, such as elastic modulus, over time rather than instantly achieving desired values post-pouring. This progressive transformation of mechanical properties is known as hydration [1]. Given the significant role of the elastic modulus, especially its temporal changes, in prompting early deformation and cracking [2], it is essential to monitor its development throughout the hydration phase.

Currently two dominant methods are used for measuring the elastic modulus of concrete: the static method and the dynamic method. Accordingly, the elastic moduli obtained through these two methods are referred to as the static elastic modulus and the dynamic elastic modulus, respectively. In the static method [3,4], a static compressive load is applied to the concrete specimen to determine the secant modulus from the stress-strain curve within the elastic range. This modulus determined through the static compression test is used in structural design as recommended by the design codes [3]. The static method is characterized by a low strain rate, resulting in a high magnitude of the viscoelastic component [5], and a high local strain magnitude, which may lead to the formation of microcracks at the

* Corresponding author at: Department of Materials, Mechanics, Management & Design, Faculty of Civil Engineering and Geosciences, Delft University of Technology, Stevinweg 1, Delft 2628 CN, the Netherlands.
E-mail address: minfei.liang@physics.ox.ac.uk (M. Liang).

https://doi.org/10.1016/j.conbuildmat.2024.139086
Received 26 August 2024; Received in revised form 17 October 2024; Accepted 5 November 2024
Available online 12 November 2024

interface between the cement paste and the aggregate [6], further increasing the residual strain. Given that the residual strain from these high local strains during the compression test can accumulate across multiple tests, the compression test-based static method is usually considered destructive [6,7]. Moreover, this method is not suitable for evaluating the elastic modulus in existing structures [8,9].

In contrast to the static method, the dynamic method is non-destructive [10] and involves higher strain rates, resulting in a lower contribution from the viscoelastic component [5]. Moreover, the absence of significant external loads in the dynamic method leads to a reduced residual strain. Consequently, it can be inferred that the elastic modulus measured using the dynamic method is higher than that obtained from the static method. However, this higher dynamic elastic modulus is not suitable for direct use in structural calculations [11]. Using the dynamic elastic modulus in structural design would result in underestimating the strain for a given stress level, as it would suggest that the material is stiffer than it actually is under static conditions. Underestimating strain gives a false sense of security regarding the concrete's capacity to resist loads, which can cause designers to overestimate the structural strength, increasing the risk of cracking or even catastrophic failure.

The dynamic method includes several approaches, such as EMM-ARM (E-modulus Measurement through Ambient Response Method) [10,12–14], the impact-echo approach [15–17], and the ultrasonic approach [18–21]. Of the three approaches mentioned, both EMM-ARM and the impact-echo approach rely on the resonant frequency of the specimen. The key distinction between these two lies in the triggering mechanism: the impact-echo method activates sample vibration using a hammer, whereas EMM-ARM relies on ambient noise for passive triggering. Since both approaches depend on the resonant frequency of the specimen, they are somewhat influenced by the geometric dimensions of the test specimen [22]. This dependency suggests that these approaches may not be ideal for estimating elastic modulus changes during field measurements on concrete structures like bridges or quay walls.

The ultrasonic approach typically involves using two ultrasonic sensors for generating and detecting elastic waves. These sensors can either be surface-mounted [20,21] or embedded within the sample itself [19]. The embedded piezoelectric sensors are often termed as smart aggregates (SAs) [23–25]. Recent studies [19–21] have utilized direct wave velocity or ballistic velocity, calculated by dividing the sensor distance by the measured arrival time, known as ultrasonic pulse velocity (UPV) [26,27], to estimate the dynamic elastic modulus. This estimation is based on the theoretical relationship between wave velocities in concrete and its mechanical properties [28,29]. In contrast to the EMM-ARM and impact-echo approach, the elastic modulus obtained through the ultrasonic approach is related to the material properties [30] and remains unaffected by the specimen or structure geometry, provided the wavelength of the elastic waves is shorter than the structural dimensions [31]. As a result, the ultrasonic approach allows for the measurement of the elastic modulus in concrete specimens with arbitrary geometries, making it preferable to the EMM-ARM and the impact-echo approach.

However, as mentioned above, the elastic modulus derived from ultrasonic wave velocity tends to be higher than the static elastic modulus, which is used in structural design as recommended by the design codes. This disparity makes the dynamic elastic modulus unsuitable for direct application in structural design, as relying on it would result in underestimating strain for a given stress level. Therefore, it becomes imperative to establish a correlation between static and dynamic moduli to bridge the gap between structural calculation and field measurement [11]. While no theoretical expression exists to define such a relationship, researchers have developed various empirical relationships between these two modulus [15,32–35]. However, it is important to note that these relationships have limited validity and necessitate consistency in mixture composition, curing conditions, and applied strain rates between the evaluated samples and those used to establish the empirical relationship.

To estimate the static elastic modulus directly using the ultrasonic approach, without involving any empirical models, this paper introduces a new signal processing technique based on direct wave interferometry (DWI) [36] to acquire relative velocity change, rather than relying on absolute velocity like UPV. The use of relative velocity change is able to establish a direct connection between static and dynamic elastic moduli, a concept that will be elaborated upon in Section 2.4. Additionally, monitoring the evolution of the elastic modulus using the direct wave component, primarily composed of P-waves, is easier to interpret than the more complex wave types found in the coda (the tail of the waveform [37]), which contains both P- and S-waves arriving at the receiver from various angles with equal strength [38] and with equilibrated energies [39,40]. Compared to UPV, the proposed signal processing technique requires only one input from the static test to convert the dynamic elastic modulus into the static one, and it does not rely on any empirical relationships. Unlike the static method, the proposed technique-enabled ultrasonic approach is non-destructive. The use of low strain levels in the ultrasonic approach allows for repeated testing on the same specimen, enabling the observation of changes due to factors such as freeze-thaw cycles [41] and chemical attacks [6]. Furthermore, compared to other dynamic approaches like EMM-ARM and the impact-echo approach, the proposed ultrasonic approach depends solely on material properties and is unaffected by specimen or structure geometry.

To verify the efficacy of the proposed signal processing technique, a set of experiments is designed wherein ultrasonic sensors embedded into concrete specimens within the temperature stress testing machine (TSTM) and the autogenous deformation testing machine (ADTM). The main reason for selecting TSTM and ADTM is that the temperature is kept constant throughout, which eliminates the impact of environmental temperature variations on wave velocity. In ADTM and TSTM, only the ultrasonic approach permits the in-situ measurement of the elastic modulus of these specimens. Subsequently, the consistency between the estimated static elastic modulus through the proposed signal processing technique and the static modulus obtained from the compression test is assessed by evaluating their performance in predicting stress evolution, with actual values being obtained from TSTM.

The structure of this paper is outlined as follows: Section 2 presents details on the concrete mixture, its mechanical properties, and the proposed signal processing technique; Section 3 offers information on the ADTM, TSTM, ultrasonic sensors, data acquisition parameters, and the measurement plan; Section 4 presents the experimental results, while Section 5 provides a discussion including suggestions for applying the proposed method.

2. Materials and methods

2.1. Concrete mixture and mechanical properties

Table 1 presents the detailed mixture design employed in this study. The cementitious material used is CEM III/B 42.5, which is manufactured by Eerste Nederlandse Cement Industrie (ENCI). This material is a promising low-carbon cementitious material comprising 30 % ordinary Portland cement (CEM I) and 70 % ground granulated blast furnace slag (GGBFS). Due to the pore-refining effects of GGBFS, it tends to exhibit greater autogenous deformation than pure ordinary Portland cement over time, potentially increasing the risk of early-age cracking [42]. Therefore, CEM III/B has been selected as the material, and the proposed

Table 1
Concrete mixture.

CEM III/B [kg/m^3]	Sand 0–4 mm [kg/m^3]	Gravel 4–16 mm [kg/m^3]	SP [kg/m^3]	w/b
320	811.8	1032	0.475	0.42

method can offer insights into the evolution of elastic modulus for analyzing early-age cracking risks.

The mean density of concrete on the 28th day is 2592 kg/m^3. The compressive strength tests were conducted on cubic samples with dimensions of 150×150×150 mm^3. The testing follow the standard NEN-EN 12390–3 [43] and is performed at 1, 3, 7, 14, and 28 days. For each compressive strength test, three samples are used. Static elastic modulus tests are conducted on prismatic samples measuring 100×100×400 mm^3, adhering to the determination of elastic modulus in compression specified in the NEN-EN 12390–13 [3]. The static elastic modulus was tested at 1, 3, 7, and 28 days, with each test involving two prismatic samples. The mean compressive strength and mean static elastic modulus are presented in Table 2.

2.2. Arrival time picker for ultrasonic pulse velocity (UPV): Akaike information criteria (AIC)

The theoretical relationship between the longitudinal wave velocity in concrete and its mechanical properties can be expressed as [30]:

$$v = \sqrt{\frac{E_d(1-\nu_d)}{\rho(1+\nu_d)(1-2\nu_d)}}, \quad (1)$$

where ρ represents the density of the concrete; E_d and ν_d correspond to the dynamic elastic modulus and dynamic Poisson's ratio, respectively; v denotes the longitudinal wave velocity and can be estimated by dividing the sensor distance by the measured arrival time. Since the sensor distance is typically considered constant when applying the UPV technique, the accuracy of the estimated dynamic elastic modulus using Eq. (1) largely depends on the precision of the arrival time picker.

In this paper, the arrival time of elastic waves is determined using the Akaike information criteria (AIC) [44]. The AIC value at n for a signal S with a length of N is defined by [44]:

$$AIC(n) = n\log\{\mathrm{var}(S[1,n])\} + (N-n-1)\log\{\mathrm{var}(S[n+1,N])\}\ , \quad (2)$$

where n ranges through all the samples in the signal. The onset point of the signal is identified as the point with the minimum AIC value, as illustrated in Fig. 1. In comparison to the picker relying on the Hinkley criterion, commonly used in commercial ultrasonic devices like Fresh-Con [45], the AIC-based picker demonstrates higher reliability and closer alignment with manual picks [46]. Nevertheless, it is essential to consider that when employing the AIC-based picker, it should be applied to a segment of the signal containing the onset point and displaying a high signal-to-noise ratio (SNR) [47]. In the following sections, the calculation of the dynamic elastic modulus through the UPV-based velocity and Eq. (1) takes the concrete density as 2592 kg/m^3, while the dynamic Poisson ratio is assumed as 0.25.

2.3. Signal processing technique for direct wave interferometry (DWI): the stretching technique

The direct wave interferometry (DWI) [36] is utilized to retrieve the relative velocity change in concrete. Unlike coda wave interferometry (CWI) [48], which primarily focuses on the tail of the waveform [37], DWI primarily focuses on the P-wave part. Fig. 2 presents a comparison of the direct wave and coda wave components in concrete. The advantage of utilizing the P-wave part for monitoring the elastic modulus

Table 2
Compressive strength and static elastic modulus.

Age [day]	1	3	7	14	28
Compressive strength [MPa]	5.09 ± 0.205	25.86 ± 0.746	44.52 ± 0.967	50.23 ± 2.722	56.12 ± 2.636
Static elastic modulus [GPa]	14.6	26.75	39.33	-	40.02

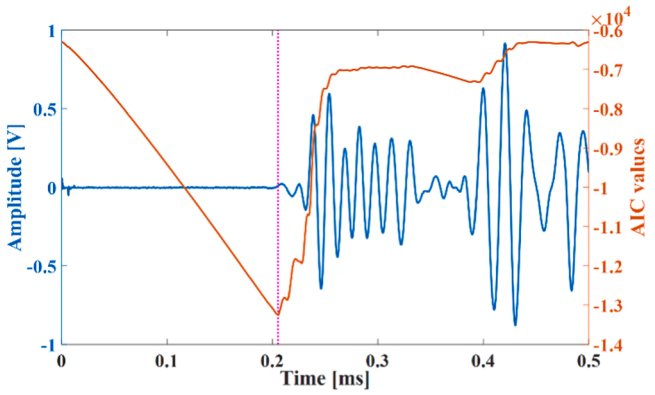

Fig. 1. AIC values and selected onset point (the pink dotted line).

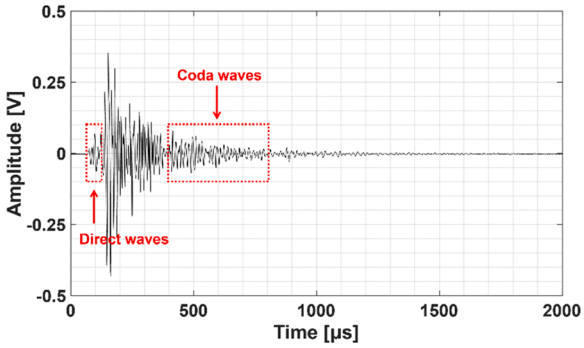

Fig. 2. Comparison of the direct wave and coda wave components in concrete.

evolution is that this part primarily consists of P-wave, which can be directly linked to mechanical properties using Eq. (1). In contrast, the coda part involves both P- and S-waves arriving at the receiver from various angles with equal strength [38] and with their energies equilibrated [39,40], creating significant difficulties in interpretation.

The stretching technique is selected as the signal processing technique for DWI. This technique is extensively utilized for determining the velocity change in seismology [49] and more recently in structural health monitoring (SHM) [50]. This technique presupposes a uniform velocity disturbance within the medium. The principle behind the stretching technique can be elucidated by the following equation [51]:

$$CC(t,T,\varepsilon) = \frac{\int_{t-T}^{t+T} u_{\mathrm{reference}}[t'(1+\varepsilon)]u_{\mathrm{current}}(t')\,dt'}{\sqrt{\int_{t-T}^{t+T}\left[u_{\mathrm{reference}}(t'(1+\varepsilon))\right]^2 dt' \int_{t+T}^{t+T}\left[u_{\mathrm{current}}(t')\right]^2 dt'}}\ , \quad (3)$$

where $u_{\mathrm{reference}}$ and u_{current} are the reference and current signals, and ε is the stretching factor. The parameter t and 2 T represent the center time and length of the time window, respectively. The parameter CC is the correlation coefficient. The stretching factor maximizes the CC is taken as the relative velocity change, dv/v. For further information on this technique, we suggest referring to the authors' previous work [51].

2.4. DWI-based static elastic modulus estimation

The dynamic elastic modulus obtained using the dynamic method is higher than the static modulus measured through mechanical testing. Although the dynamic method is non-destructive and suitable for field measurements, using the dynamic elastic modulus in structural design could result in underestimating the strain for a given stress level. This underestimation may lead designers to overestimate the structural strength, increasing the risk of cracking or even catastrophic failure. In contrast, mechanical testing is destructive and unsuitable for field measurements. To bridge the gap between structural calculations and

field measurements, it is imperative to establish a correlation between static and dynamic moduli [11].

Early studies commonly employed linear models [32,33] to characterize this relationship. However, as more experiments were conducted, it became evident that such a linear relationship lacked sufficient accuracy, especially when the static elastic modulus fell below 10 GPa. In response to this realization, nonlinear models [15,34] were proposed to better capture this relationship. Table 3 presents four representative models, encompassing two linear and two nonlinear ones. It is crucial to emphasize that these models are only applicable to a limited range of concrete types and mixtures. Details regarding the applicable concrete types can be found in Appendix B. For example, the values of a and b involved in the model presented by Han & Kim [15] are determined for specimens with two specific concrete mixture compositions. For concrete with a different mixture composition, the proposed a and b in their article are not applicable. Therefore, a generalized model for the relationship between static and dynamic elastic moduli is needed to link these two moduli through velocity changes retrieved using the stretching technique.

Fig. 3 visually delineates the distinctions among the models under discussion. In the model presented by Han & Kim [15], the parameters a and b are assigned as 0.772 and 0.0301, respectively. These values correspond to a mixture composition with water-cement ratio of 0.4 and a curing temperature of 23℃. Below 10 GPa, the nonlinear expressions exhibit substantial nonlinearity, as depicted in Fig. 3(a). However, when the static elastic modulus exceeds 30 GPa, the correlation between static and dynamic elastic moduli among various nonlinear models tends to approximate linearity, as shown in Fig. 3(b). While acknowledging the influence of wave frequency on the derived dynamic elastic modulus [52], it is anticipated that for static elastic moduli exceeding 30 GPa, the relationship between static and dynamic elastic moduli will tend towards linearity for ultrasonic waves with consistent frequency components [53]. This understanding can be further used to propose a generalized linear expression when addressing static elastic moduli within this range.

Based on the finding in Fig. 3, this paper employs a generalized linear expression to depict the correlation between static and dynamic elastic moduli when the static modulus surpasses 30 GPa. Rather than depending on a particular model with predetermined parameters, this generalized expression provides adaptability in capturing the connection between the two moduli. The linear model can be articulated as:

$$E_c = \alpha E_d + \beta \ , \tag{4}$$

where α and β are two parameters describing the linear relationship between static and dynamic elastic moduli. These two parameters can be determined by performing a linear fit on the curves shown in Fig. 3(b) and are shown in Table 4.

A relative dynamic elastic modulus, denoted by $E_d^{(relative)}$, is defined as the ratio between the current measurement $E_d^{(current)}$ and the measurement obtained on the 28th day $E_d^{(28)}$:

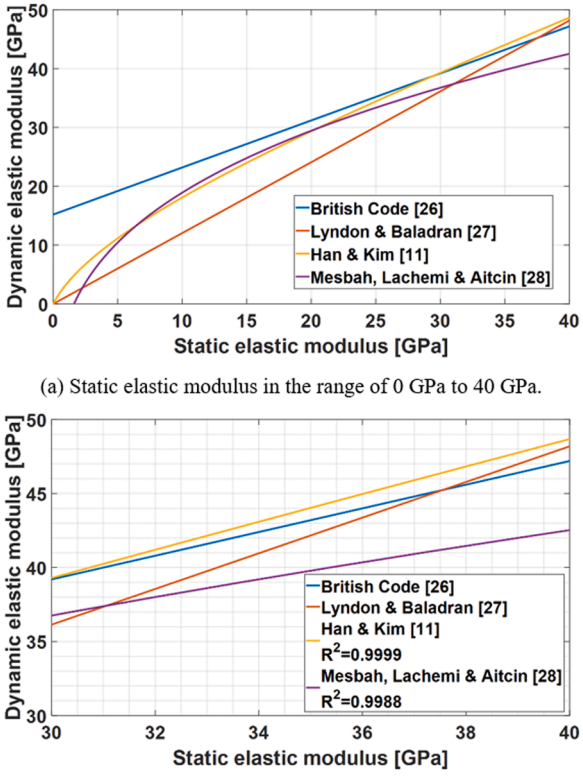

(a) Static elastic modulus in the range of 0 GPa to 40 GPa.

(b) Static elastic modulus in the range of 30 GPa to 40 GPa.

Fig. 3. Relationship between static and dynamic elastic modulus of concrete proposed by: British Code BS 8110–2: 1985 [32], Lyndon & Baladran [33], Han & Kim [15], and Mesbah, Lachemi & Aitcin [34].

Table 4
Linear fit parameters, α and β, using Eq. (4) for models in Table 3.

Model type	Authorship	Parameter values		R^2 between model outputs and linear fit
		α	β	
Linear	BS 8110–2: 1985 [32]	1.25	−19	1.0000
	Lyndon & Baladran [33]	0.83	0	1.0000
Nonlinear	Mesbah, Lachemi & Aitcin [34]	1.724	−33.43	0.9988
	Han & Kim [15]	1.066	−11.9	0.9999

Table 3
Four representative models for the relationship between static elastic modulus E_c and dynamic elastic modulus E_d.

Model type	Linear		Nonlinear	
Authorship	BS 8110–2: 1985 [32]	Lyndon & Baladran [33]	Mesbah, Lachemi & Aitcin [34]	Han & Kim [15]
Relation between E_c and E_d	E_c=1.25E_d−19	E_c=0.83E_d	E_c=9×10^{-11}(65E_d+1600)$^{3.2}$	E_c=E_d(1-a×e$^{-b\times Ed}$)
Applicable concrete type/mixture	Normal aggregate concrete	Appendix B Table B1	Appendix B Table B2	Appendix B Table B3

$$E_{\mathrm{d}}^{(\mathrm{relative})} = \frac{E_{\mathrm{d}}^{(\mathrm{current})}}{E_{\mathrm{d}}^{(28)}} = \frac{\frac{E_{\mathrm{c}}^{(\mathrm{current})} - \beta}{\alpha}}{\frac{E_{\mathrm{c}}^{(28)} - \beta}{\alpha}} = \frac{E_{\mathrm{c}}^{(\mathrm{current})} - \beta}{E_{\mathrm{c}}^{(28)} - \beta} = \left[1 + \frac{\beta\left(E_{\mathrm{c}}^{(\mathrm{current})} - E_{\mathrm{c}}^{(28)}\right)}{E_{\mathrm{c}}^{(\mathrm{current})}\left(E_{\mathrm{c}}^{(28)} - \beta\right)}\right]\frac{E_{\mathrm{c}}^{(\mathrm{current})}}{E_{\mathrm{c}}^{(28)}} \quad . \tag{5}$$

As shown in Eq. (5), the parameter α is eliminated and will not affect the relative dynamic elastic modulus. In addition, the relative dynamic elastic modulus can be obtained through the relative static elastic modulus by multiplying a coefficient $1 + \beta\left(E_{\mathrm{c}}^{(\mathrm{current})} - E_{\mathrm{c}}^{(28)}\right)/E_{\mathrm{c}}^{(\mathrm{current})}\left(E_{\mathrm{c}}^{(28)} - \beta\right)$. To quantify the impact of this term on the relationship in Eq. (5), we select the static elastic modulus on the 7th day from Table 2, which is 39.33 GPa, as the current measurement of static elastic modulus, $E_{\mathrm{c}}^{(\mathrm{current})}$. The static elastic modulus on 28th day, $E_{\mathrm{c}}^{(28)}$, is 40.02 GPa. We assign the parameter β to a magnitude of −34, which corresponds to the model proposed by Mesbah, Lachemi & Aitcin [34]. Substituting these values into Eq. (5) yields the following expression:

$$E_{\mathrm{d}}^{(\mathrm{relative})} = 1.008\frac{E_{\mathrm{c}}^{(\mathrm{current})}}{E_{\mathrm{c}}^{(28)}} \approx \frac{E_{\mathrm{c}}^{(\mathrm{current})}}{E_{\mathrm{c}}^{(28)}} \quad . \tag{6}$$

Please note that the magnitude of the mentioned coefficient, $1 + \beta\left(E_{\mathrm{c}}^{(\mathrm{current})} - E_{\mathrm{c}}^{(28)}\right)/E_{\mathrm{c}}^{(\mathrm{current})}\left(E_{\mathrm{c}}^{(28)} - \beta\right)$, will be smaller if other β values from Table 4 are selected. Eq. (6) showcases that as the static elastic modulus reaches a plateau in its development, the relative static elastic modulus can be described in terms of the relative dynamic elastic modulus. If we take a current static elastic modulus of 30 GPa and maintain the same value for the parameter β and static elastic modulus on 28th day, the coefficient in Eq. (6) will increase from 1.008 to 1.153. This suggests that representing the relative static elastic modulus directly using the relative dynamic elastic modulus in this scenario may result in an overestimation of around 13 %, which is considered as a worst scenario according to the β values provided in Table 4.

The relative dynamic elastic modulus is obtained through the DWI approach, which measures wave velocity as a relative change rather than an absolute value. The change in velocity can be formulated as a function involving the dynamic elastic modulus, dynamic Poisson's ratio, and concrete density, expressed as follows:

$$\frac{\mathrm{d}v}{v} = \frac{v^{(i+1)} - v^{(i)}}{v^{(i)}} = \frac{\sqrt{\frac{E_{\mathrm{d}}^{(i+1)}\left(1-\nu_{\mathrm{d}}^{(i+1)}\right)}{\rho^{(i+1)}\left(1+\nu_{\mathrm{d}}^{(i+1)}\right)\left(1-2\nu_{\mathrm{d}}^{(i+1)}\right)}} - \sqrt{\frac{E_{\mathrm{d}}^{(i)}\left(1-\nu_{\mathrm{d}}^{(i)}\right)}{\rho^{(i)}\left(1+\nu_{\mathrm{d}}^{(i)}\right)\left(1-2\nu_{\mathrm{d}}^{(i)}\right)}}}{\sqrt{\frac{E_{\mathrm{d}}^{(i)}\left(1-\nu_{\mathrm{d}}^{(i)}\right)}{\rho^{(i)}\left(1+\nu_{\mathrm{d}}^{(i)}\right)\left(1-2\nu_{\mathrm{d}}^{(i)}\right)}}} \quad , \tag{7}$$

where i represents the i^{th} measurement of the wave signal, v denotes the longitudinal wave velocity, and ρ represents the density of the concrete. The parameters E_{d} and ν_{d} correspond to the dynamic elastic modulus and dynamic Poisson's ratio, respectively. Supposing that the density and dynamic Poisson's ratio remain relatively constant during concrete hydration, an acceptable assumption for concrete after 7 days of casting [54,55], and integrating Eq. (6), Eq. (7) can be elaborated as:

$$\frac{E_{\mathrm{c}}^{(i+1)}}{E_{\mathrm{c}}^{(i)}} \approx \frac{E_{\mathrm{d}}^{(i+1)}}{E_{\mathrm{d}}^{(i)}} \approx \left(\frac{v^{(i+1)} - v^{(i)}}{v^{(i)}} + 1\right)^2 \quad . \tag{8}$$

As shown in Eq. (8), employing the linear generalized model within the range of elastic modulus beyond 30 GPa can help eliminate the parameter β in Eq. (4)—related to factors such as curing temperature and mixture composition—and directly estimate the static elastic modulus from velocity changes retrieved using the stretching technique. By knowing the magnitude of static elastic modulus on the 28th day using the compression test, denoted as $E_{\mathrm{c}}^{(28)}$, we can calculate the progression of the static elastic modulus using the subsequent expressions:

$$E_{\mathrm{c}}^{(i)} = E_{\mathrm{c}}^{(i+1)}\left(\frac{v^{(i+1)} - v^{(i)}}{v^{(i)}} + 1\right)^{-2} \quad , \tag{9a}$$

$$E_{\mathrm{c}}^{(j)} = E_{\mathrm{c}}^{(j-1)}\left(\frac{v^{(j)} - v^{(j-1)}}{v^{(j-1)}} + 1\right)^{2} \quad . \tag{9b}$$

where i represents the measurement taken before 28 days of casting, while j denotes the measurement taken after 28 days of casting.

3. Experimental setup

3.1. Temperature stress testing machine (TSTM) and autogenous deformation testing machine (ADTM)

The temperature stress testing machine (TSTM) is a universal testing device designed to characterize and quantify the thermo-mechanical properties of early-age cementitious materials under controllable mechanical and thermal conditions. With various boundary settings, the TSTM can be used to measure not only stress evolution but also elastic modulus, creep/relaxation, coefficient of thermal deformation, and autogenous/thermal deformation—all of which are critical metrics for evaluating early-age cracking risks. In the TSTM setup, the specimen takes the shape of a dog bone, which imposes deformation restraint, enabling the load cell to capture the evolution of restraint stress. For the autogenous deformation testing machine (ADTM) setup, the prism-shaped specimen is cast in a wooden mold characterized by low thermal conductivity. Since the specimen is free to deform, autogenous shrinkage can be measured using linear variable differential transformers (LVDTs). Both ADTM and TSTM tests are conducted under isothermal conditions, where the temperature is maintained at a constant 20°C through active water circulation. This temperature control is crucial, as temperature variations can also affect wave velocity in concrete. For readers interested in these two test setups, a detailed review of the TSTM and ADTM can be found in the paper [56].

Fig. 4 demonstrates the ADTM setup used for testing the autogenous deformation of concrete. Wood plates with curved water channels (Fig. 4 (b)) are assembled to create a mould for casting prismatic samples measuring 1250×150×100 mm^3 (Fig. 4(a)). A steel plate is affixed to the inner surface of the wood mould to facilitate rapid heat conduction (Fig. 4(c)). Temperature-regulated water circulates around the wood mould to control the temperature, guided by feedback from thermocouple embedded in the sample (indicated by the dot in Fig. 4(a)). Four LVDTs (Fig. 4(d)) are positioned on both sides of the sample to measure the average deformation. To mitigate the impact of thermal deformation of the base, a quartz bar is used to connect LVDTs on each side.

Fig. 5 portrays the TSTM setup, comprising a dog-bone mould with a prismatic testing area of interest (1000×150×100 mm^3) and an actuator designed to confine autogenous deformation and measure stress development under displacement-controlled boundaries. The assembly of the mould, temperature control, and LVDT configurations align with the principles described for ADTM. Four LVDTs are situated at the middle

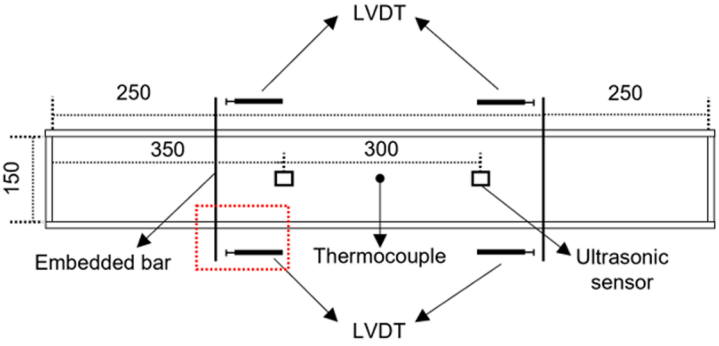

(a) ADTM schematic diagram (unit: mm) (red rectangle will be shown in Figure 4(d)).

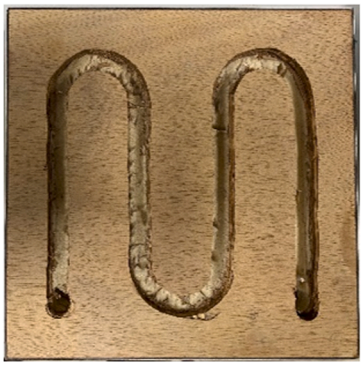

(b) water channel.

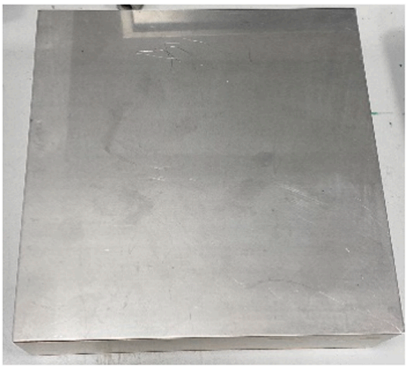

(c) Insulation and conduction plate.

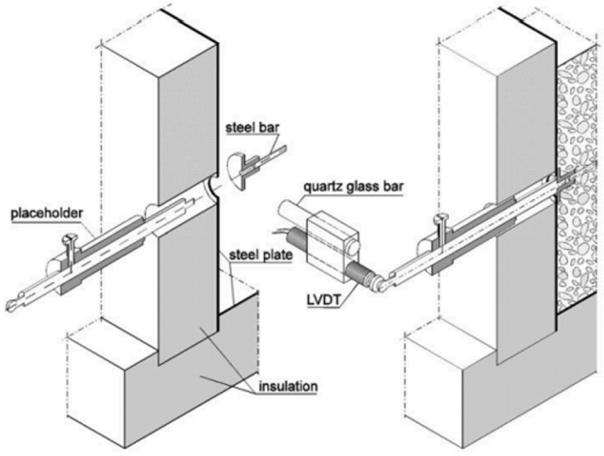

(d) Embedded bar and LVDT holder (red rectangle in Figure 4(a)).

(e) Photo of ADTM setup.

Fig. 4. Autogenous Deformation Testing Machine (ADTM).

section of the dog-bone sample, enabling continuous force application to maintain the average deformation at zero. To ensure the capture of all autogenous deformation-induced stress during the experiment, the test should promptly start after the concrete has hardened. In this study, the TSTM test was initiated approximately 7 hours after casting, preceding the setting time of the cement paste studied. Before setting the LVDTs, the load was controlled based on the displacement of the clamping head. During the initial phase, when the concrete had not completely solidified (within the first 7 hours after casting), the measured stress remained below 0.01 MPa. Hence, only stress values recorded after the 7-hour mark were considered in the experimental results presented in this paper.

3.2. Ultrasonic sensors and their locations

As shown in Section 3.1, for the samples in the ADTM and TSTM setups, it is challenging to install the ultrasonic sensors on the surface of the sample. Therefore, to generate and detect elastic waves in concrete, the ultrasonic sensors with a resonant frequency of approximately 80 kHz [57] are embedded inside the concrete samples. The sensing element of this sensor is lead zirconate titanate (PZT) in d_{33} mode, which is delicate and susceptible to damage when in direct contact with fresh

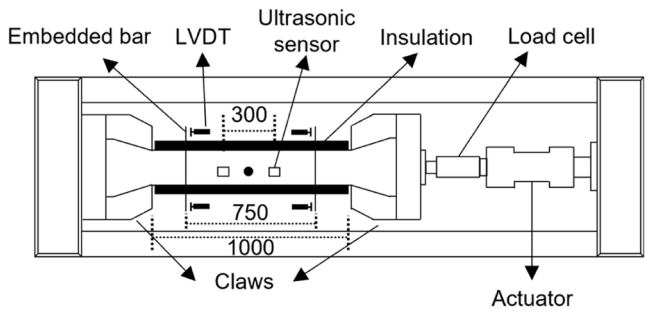

(a) TSTM schematic diagram (unit: mm).

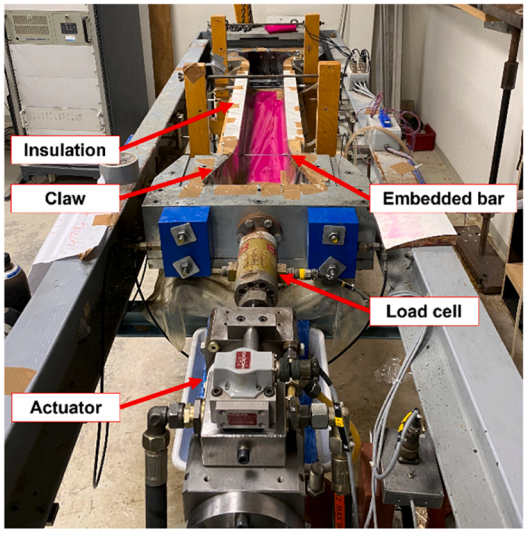

(b) Photo of TSTM setup.

Fig. 5. Temperature Stress Testing Machine (TSTM).

concrete. Therefore, to protect the fragile PZT element, two marble blocks are utilized to encase and shield it. A visual representation of an ultrasonic sensor used in this paper is depicted in Fig. 6(a), while further details about this sensor can be found in [25]. The use of embeddable ultrasonic sensors can also facilitate the application of the stretching technique, as this method requires minimal environmental variation and strong coupling. In ADTM, two ultrasonic sensors, fixed using a U-shaped copper wire, are embedded in the specimen, spaced at a distance of 300 mm, as shown in Fig. 4(a). Similarly, in TSTM, two sensors are installed in the sample with the same 300 mm spacing, as shown in Fig. 5(a). The height of sensors in both ADTM and TSTM is 50 mm. The photo of ultrasonic sensors in the TSTM setup can be found in Fig. 6(b).

To generate and capture wave signals, a portable ultrasonic device with one input channel and one output channel is employed. An excitation signal in the form of a one-cycle squared pulse with a duration of 18.5 μs is utilized, which corresponds to around 54 kHz. This frequency is close to the resonant frequency of embedded ultrasonic sensors, which is around 80 kHz. Additionally, waves at this frequency are expected to experience less attenuation compared to those above 100 kHz, resulting in a better signal-to-noise ratio. The wavelength of longitudinal waves at 54 kHz is approximately 83 mm, which is shorter than the cross-sectional dimensions of the specimen (150 mm by 100 mm). The sensor spacing of 300 mm corresponds to around 3.6 wavelength, allowing accurate detection of individual wave cycles. The minimum distance from the sensor to the surface of the specimen is 50 mm. Considering that the frequency of the pulse is 54 kHz and the surface Rayleigh wave velocity in concrete is around 2300 m/s [58], the maximum effective depth of penetration of Rayleigh waves is about 43 mm [59]. Since this is smaller than 50 mm, Rayleigh wave-related

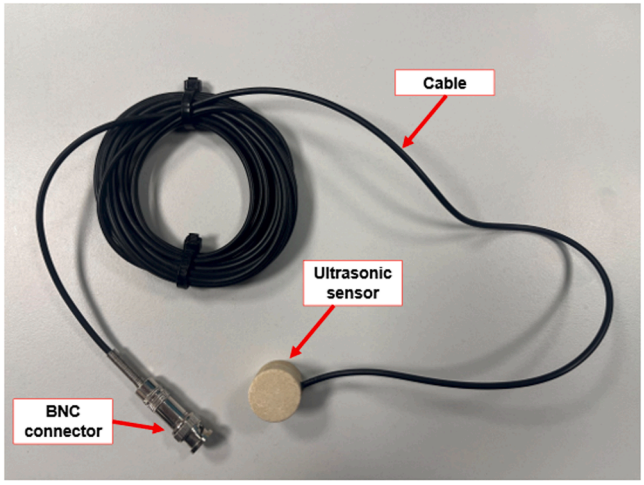

(a)

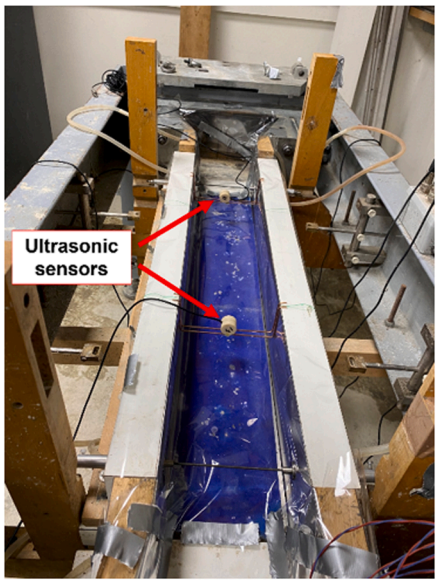

(b)

Fig. 6. Ultrasonic sensor used in this paper. (a) A photo of an ultrasonic sensor. The sensor is a P-wave sensor with a cylindrical shape. The diameter of the sensor is 25 mm, and its height is 20 mm. The sensing element is a d_{33} mode PZT patch with a polarization direction aligned along the height direction. The resonant frequency of the sensor is approximately 80 kHz. (b) A photo of ultrasonic sensors installed in the TSTM setup. Please note that this picture was taken when the sensors were initially placed into the mould. The sensor locations were adjusted according to Fig. 5(a) before casting the concrete.

particle velocities in our measurements can be neglected.

The chosen sampling rate is 1 MHz, which is more than ten times the frequency of the pulse, ensuring accurate waveform capture. Please note that even though we adopt embedded sensors in the experiment, the proposed DWI-based ultrasonic approach in Section 2.4 can also be used to process the signals received by surface-bonded ultrasonic sensors. This aspect will be further discussed in Section 5.

3.3. Ultrasonic measurements

Since velocity variation during the hydration process follows a pattern of rapid increase in the early stages and, followed by a slowdown as curing time progresses [1], the measurement intervals during ultrasonic testing are not constant. More measurements are taken during the

early stages, with fewer in the later stages. Because the ultrasonic device used for data acquisition has only one input and one output channel, the ADTM and TSTM specimens cannot be monitored simultaneously. As a result, we focused primarily on measuring signals from the TSTM specimen by setting specific intervals that allow the ultrasonic device to collect data automatically.

For the concrete sample hydration monitoring in the TSTM, measurements commenced 0.63 hours after casting and continued at 10-minute intervals until 168 hours (7 days). The first reading was taken 0.63 hours (around 40 minutes) after casting as this time was needed to set up the moulds and prepare the loading and water circulation systems. Subsequently, from 168 hours to 336 hours (14 days), measurements were taken every hour. Due to negligible velocity change post-336 h, the interval was adjusted to 2 hours until 504 hours (21 days). Notably, there was a lapse in measurements between 16 and 19 days after casting during the ultrasonic device inspection, even though the test was ongoing. The interval was further extended to 6 hours between 504 hours and 744 hours (31 days) and then set to 12 hours for the final stage from 744 hours to 840 hours (35 days). Fig. 7(a) presents the measurement points and corresponding curing times for the sample in the TSTM setup. Please be aware that the time intervals may not precisely match the aforementioned values in each stage, as indicated in Fig. 7(b). This discrepancy primarily arises because manual checks were conducted following specific number of measurements to assess waveform changes and ensure the functionality of the ultrasonic system.

The same ultrasonic device was employed for data acquisition in the ADTM sample. However, measurements were performed during manual checks, as explained in the previous paragraph and shown in Fig. 7(b). Consequently, the total number of measurements for the ADTM sample is much lower than that for the TSTM sample. Due to the limited number of measurements in the ADTM sample, they are primarily utilized to verify the reliability of the measurements obtained in the TSTM sample. The initial measurement for the sample was conducted approximately 11.41 hours after casting, with the final measurement occurring around 840 hours. Throughout this period, a total of 32 measurements were taken. The curing time corresponding to each measurement point is illustrated in Fig. 8.

4. Results

4.1. Determination of the hydration stage in terms of signal amplitude

In this section, the signals collected from the TSTM specimen are primarily used, as this specimen boasts a denser array of measurement

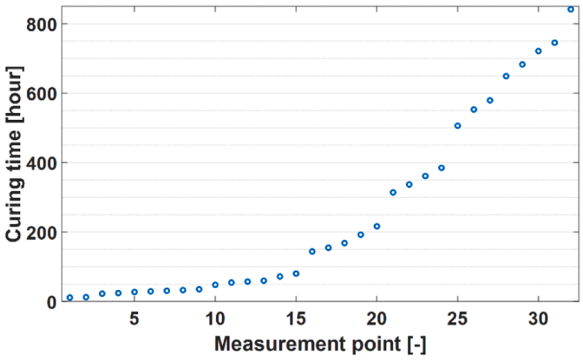

Fig. 8. Ultrasonic measurements in the ADTM specimen.

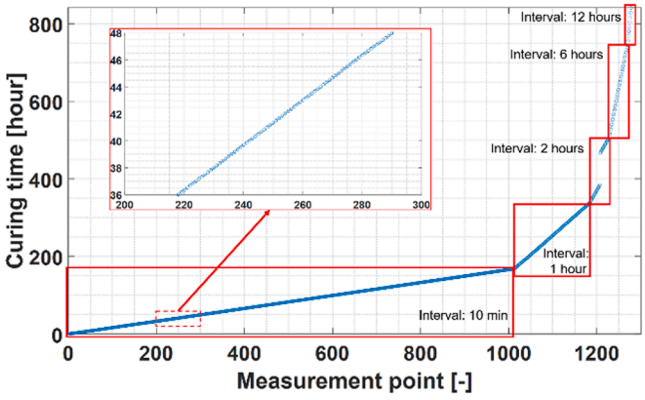

(a) Measurement point vs curing time.

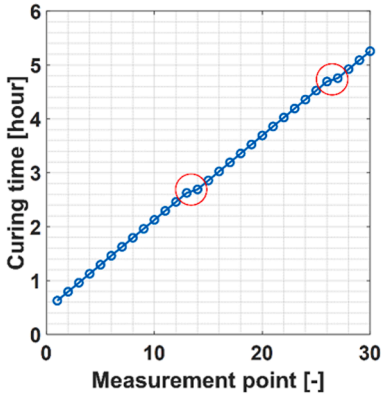

(b) Fluctuation in time interval due to manual check during data acquisition marked using red circles.

Fig. 7. Ultrasonic measurements in the TSTM specimen.

points compared to the ADTM specimen. The first measurement was taken around 40 minutes post-casting, and Fig. 9 portrays five representative signals obtained before the 7.00-hour mark. The initial velocity of the measurement is approximately 1400 m/s, slightly lower than the wave velocity in water (1430 m/s), owing to the air-water system, as detailed in [60]. Initially, the received signal amplitudes are high and gradually diminish over time, aligning with observations in [61,62]. A possible explanation is that, during this stage, the solid network is developing [1], transforming the concrete into a water-solid system. As the wave propagates through this two-phase material, it undergoes significant interactions between the phases, leading to faster signal attenuation. This initial stage of hydration is recognized in the literature as the dormant stage [1].

Fig. 10 illustrates the cessation of received signals around 8.50 hours, a phenomenon observed in previous studies utilizing SA for hydration monitoring [61,63]. The re-emergence of a signal at approximately 10.06 hours (as seen in Fig. 10) signifies the interconnection of the solid frame between two SAs, recognized as the solid percolation threshold [64]. This marks the transition from the dormant stage to the acceleration stage [1].

Following the reappeared signal, there is a significant increase in signal energy and wave velocity over the subsequent 14 hours, as displayed in Fig. 11(a). Please be aware that the time intervals in Fig. 11 may not precisely match the aforementioned values in Section 3.3, which has been explained above. In Fig. 11(a), particularly for the signals collected before 15 hours, the SNR is extremely low. Some researchers in the literature have recommended manual picking over automatic methods during this stage [65], although manual picking may introduce subjective errors. Notably, Fig. 11(a) also showcases the absence of a distinct S-wave component in the waveform 24 hours after casting, while Fig. 11(b) illustrates signals commencing with low amplitudes and then experiencing a sudden increase at around 150 μs, indicative of the presence of the S-wave in the waveform. In Fig. 11(c), the P-wave amplitude begins to stabilize after 54 hours, with the latter segment of the waveform—starting from roughly 140 μs—comprising both P-wave and S-wave components, continues to display growth. This growth of signal energy, primarily attributed to the growth of S-wave energy, is associated with the enhanced ability to transfer shear stress within the medium during early solid percolation [64,66]. Hence, it can be deduced that the shear modulus development lags slightly behind the elastic modulus, consistent with observations in [67]. The waveform amplitude stabilizes after 105 hours (Fig. 11(d)), and only a marginal phase difference is noticed between different measurements after 168 hours, depicted in Fig. 11(e) and Fig. 11(f). It is important to note the challenge in identifying the second turning point, denoting the transition to the deceleration stage where all individual solid phases interconnect [1], using the sensor setup employed in this study. Given the utilization of only a single sensor pair, the investigation is confined to the region between two SAs rather than encompassing the entire sample, making the detection of interconnection of all solid phases challenging.

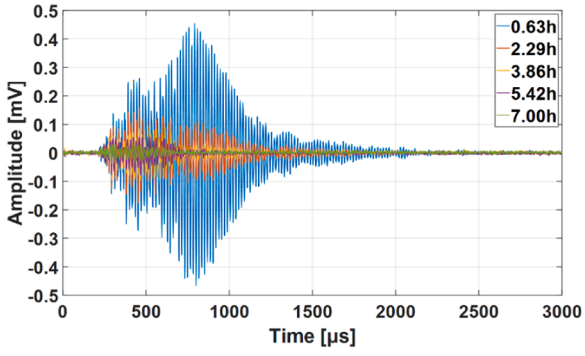

Fig. 9. Received signals in TSTM before 7 hours. The signal amplitude is highest at beginning (0.63 h) and gradually decrease over time.

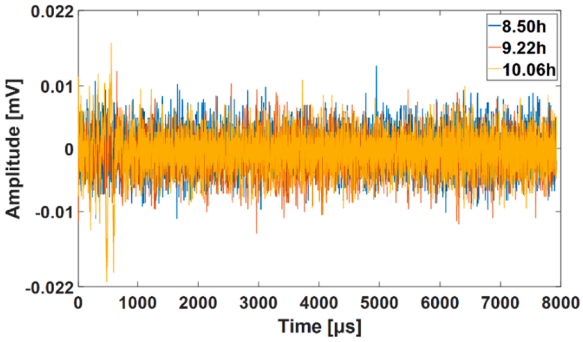

Fig. 10. Received signals in TSTM from 8.5 hours to 10 hours. There are no discernible signals between 8.50 h and 9.22 h. At 10.06 h, a higher amplitude vibration occurs at around 500 μs, which appears to mark the re-emergence of the signal.

4.2. Comparison between wave velocities measured using UPV and DWI

To compare velocities obtained from the UPV and DWI techniques, the AIC picker is employed to determine the onset point for UPV, with primary focus on velocity measurements after 13.42 hours, where a clear onset point becomes discernible. For DWI, the stretching technique is utilized in the P-wave portion with a window length of 50 μs. Notably, the application of the stretching technique follows a stepwise approach, using the preceding signal as the reference. Consequently, the resulting relative velocity change is also stepwise. In some literature [68], researchers employ accumulated velocity changes to establish an overall velocity change relative to the initial state. However, this approach suits minor velocity perturbations, such as stress-induced or temperature-induced velocity changes. In the context of the substantial velocity increment observed in Fig. 11(b), direct utilization of accumulated velocity change would significantly underestimate the actual velocity change.

The approach adopted in this section is similar to that presented in [69]. Instead of accumulating all velocity changes, the velocity at each measurement point is constructed using relative velocity changes. A particular caution is required during a specific step in this process: the denominator term in the velocity change (dv/v) derived from the stretching technique relies on the selected stretched/compressed signal. In this study, the reference signal is consistently stretched. Assuming t_0, t_1, v_0, and v_1 represent the arrival time and velocity of the reference and current signals, respectively, the relationship between dt/t and dv/v obtained through stretching with the reference signal stretched can be articulated using the following equation:

$$\frac{dt}{t} = \frac{t_0 - t_1}{t_1} = \frac{\frac{1}{v_0} - \frac{1}{v_1}}{\frac{1}{v_1}} = \frac{v_1 - v_0}{v_0} = \frac{dv}{v} \quad . \tag{10}$$

Hence, in this study, the stepwise velocity change is expressed as $(v_{i+1}\text{-}v_i)/v_i$, where i ranges from 1 to the number of received signals minus 1. Replacing the denominator term v_i with v_{i+1} can result in erroneous outcomes. To construct the velocity from the stepwise velocity change, a three-step approach is employed:

1. Converting the relative velocity change, $(v_{i+1}\text{-}v_i)/v_i$, into relative velocity, v_{i+1}/v_i.

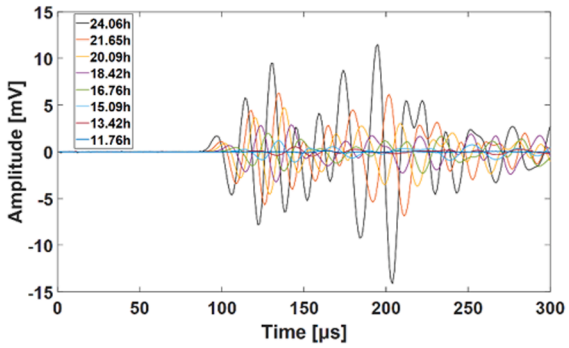

(a) Received signals from 10 hours to 24 hours. The signal amplitude is extremely low before 15h.

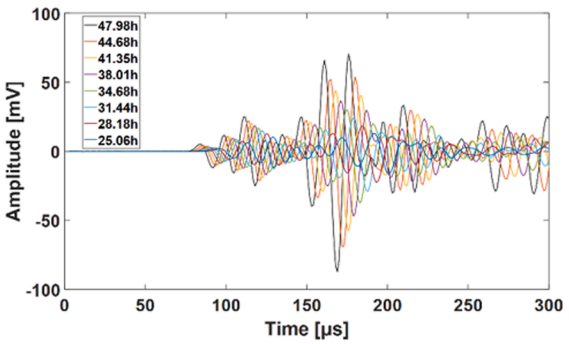

(b) Received signals from 24 hours to 48 hours. A clear increase in both velocity and amplitude over time can be observed.

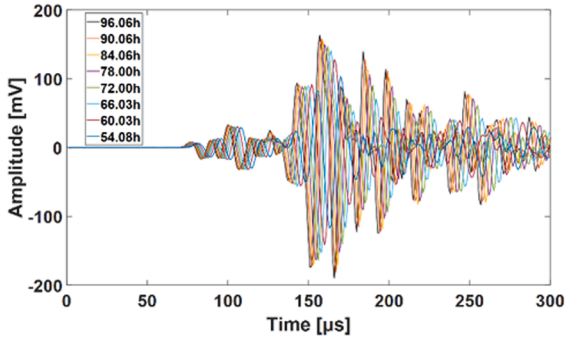

(c) Received signals from 48 hours to 96 hours. The amplitude changes of the P-wave component (before 140 μs) over time reach a plateau, while those of P- and S-wave component (after 140 μs) continue to increase dramatically.

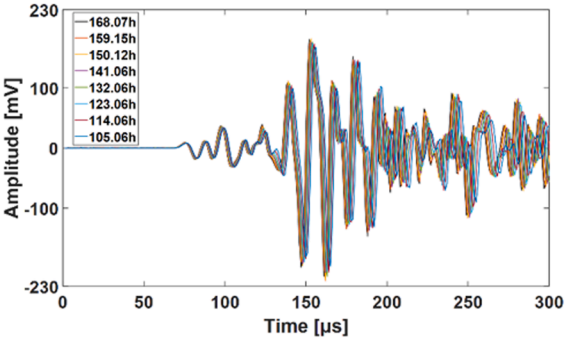

(d) Received signals from 96 hours to 168 hours. The velocity changes are less pronounced, and the amplitude of P- and S-wave component (after 140 μs) remains stable over time.

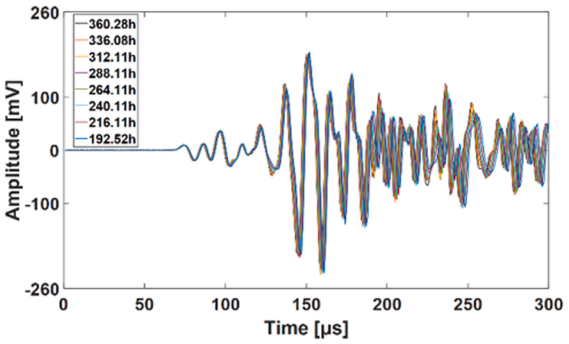

(e) Received signals from 168 hours to 360 hours. There is slight increase in velocity, and signal amplitudes are stable.

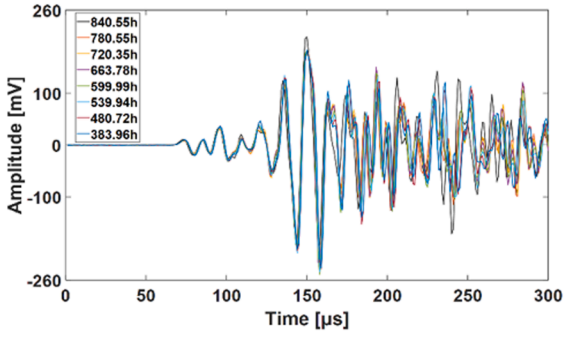

(f) Received signals from 360 hours to 840 hours. There is slight increase in velocity, and signal amplitudes are stable.

Fig. 11. Received signals in TSTM from 10 hours to 840 hours.

2. Calculating the wave velocity in the last measurement, 840 hours (35 days) after casting, using the AIC approach, as this signal theoretically exhibits the best SNR.
3. Estimating the velocities at each measuring point using the relative velocity and the absolute velocity from UPV in the last measurement.

Fig. 12 illustrates the fluctuation in relative velocity during the hydration process. Approximately 10 hours after casting, a noticeable decline in the *CC* value is observed, signifying the transition from the dormant stage to the acceleration stage. In instances where the signals exhibit extremely low SNR, the reliability of dv/v might be compromised due to potential cycle skipping. Thus, in this section, only dv/v values

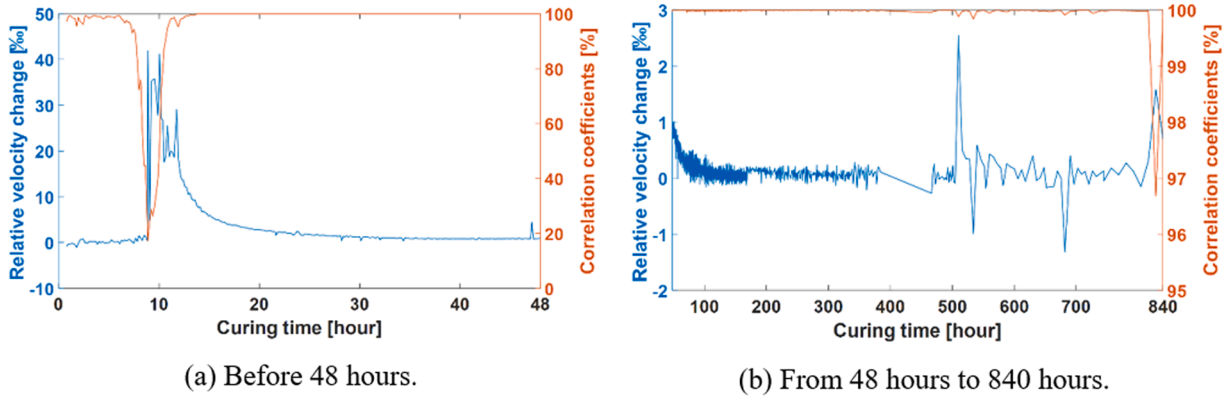

Fig. 12. Relative velocity change and correlation coefficients in TSTM.

with a *CC* value exceeding 0.9 are used to ensure data reliability. Subsequently, after 48 hours, the dv/v values reach a relatively stable state.

Fig. 13 presents a comparison between DWI-based constructed velocities and UPV results. The constructed velocities exhibit good agreement with the UPV results and showcase enhanced resolution due to signal correlation operations. While achieving the same resolution as DWI theoretically by increasing the sampling rate of UPV signals is possible, this would require a more advanced data acquisition device and additional storage space, proving economically impractical for field measurements.

4.3. Comparison between wave velocities in TSTM and ADTM

In Fig. 12(a), we pointed out that velocity changes with low *CC* values may lack reliability. To validate the reliability of DWI-based constructed velocities beyond 13.42 hours, we compared them with the UPV results in Fig. 13. Therefore, before further analysis using DWI-based constructed velocities, it is crucial to verify the trustworthiness of velocities constructed before 13.42 hours.

Fig. 14 illustrates the DWI-based constructed velocity, covering the period before 13.42 hours. According to the estimation, the velocity of the initial measurement (0.63 hours after casting) stands at 1416 m/s, with an associated arrival time of approximately 212 μs. The waveform of the first measurement is shown in Fig. 15, with the picked arrival time by AIC marked at 214 μs. With a sampling rate of 1 MHz, the error amounts to two sampling points, which is deemed acceptable for this application. Consequently, the velocities obtained before 13.42 hours can be considered reliable.

It is noteworthy that a rapid development of P-wave velocity is observed at around 8.8 hours, as indicated by the red dot in Fig. 14. According to Azenha et al. [70], this rapid increase in velocity signifies the moment when final setting occurs. Additionally, the evolution of the

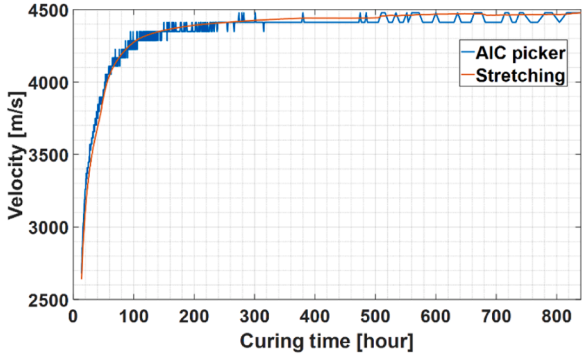

Fig. 13. Comparison between AIC-based UPV and DWI-based constructed velocity (after 13.42 h) in TSTM.

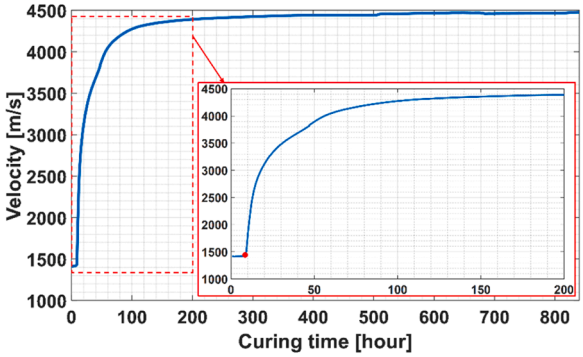

Fig. 14. DWI-based constructed velocity in TSTM. The red dot in this figure signifies the moment when final setting occurs, marking the rapid increase of P-wave velocity, which begins at approximately 8.8 hours.

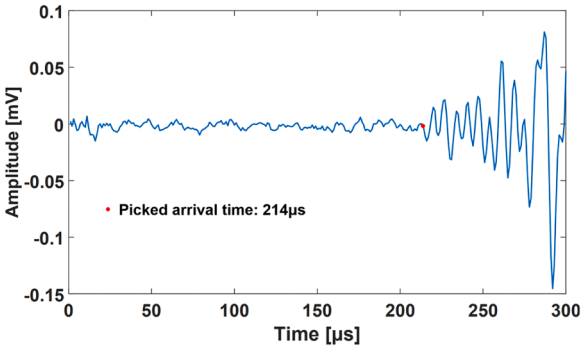

Fig. 15. The first received signal at 0.63 hours in TSTM.

constructed velocity during the hydration process aligns with findings reported in the literature [1]. The precise transition point from the acceleration stage to the deceleration stage remains challenging to determine. However, the velocity observed around 200 hours (as depicted in the zoomed section of Fig. 14) suggests that the wave velocity has reached a plateau by that time.

The development of velocity in the ADTM is constructed using the methodology outlined in Section 4.2. To normalize the velocity evolution and mitigate distance errors from manually installed sensors, the relative velocity with the wave velocity on the 28th day after casting serving as the reference is utilized. The comparison between velocities measured in the TSTM and ADTM setups is presented in Fig. 16. In the ADTM setup, the concrete sample can freely shrink without deformation constraints. In contrast, in TSTM, the presence of stress might slightly

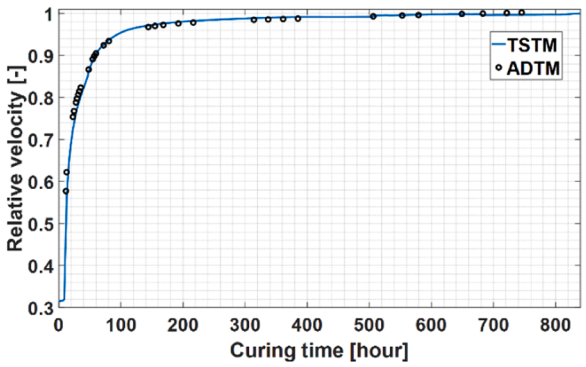

Fig. 16. DWI-based constructed relative velocity with 28th day as reference in TSTM and ADTM.

alter the wave velocity due to acoustoelasticity [71]. However, Fig. 16 demonstrates a high similarity between the developments of wave velocity in TSTM and ADTM. Given that one of the primary distinctions between ADTM and TSTM is the different restrained conditions, the similar velocity developments suggest that, especially during the early stage before 200 hours, the change in wave velocity is primarily influenced by concrete hydration rather than shrinkage-induced stress.

4.4. DWI-based static elastic modulus estimation

The calculation of the relative elastic modulus to the 28th day, follows the approach outlined in Section 2.4. To convert the relative value into an absolute value, the static elastic modulus obtained from the prism compression test on the 28th day is used as input into the relative modulus curve. Fig. 17 showcases a comparison between DWI-based static elastic modulus estimation, UPV-based dynamic elastic modulus, and prism compression test-based static elastic modulus.

As discussed in Section 4.1, the reappeared signal is observed approximately 10 hours after casting. Thus, only the elastic moduli after 10 hours are used in this section. The elastic moduli estimated using DWI on days one, three, and seven are 21.77 GPa, 34.42 GPa, and 38.29 GPa, respectively. The associated relative errors, compared to static elastic moduli measured via compression tests, are 49.1 %, 28.7 %, and 2.6 %. In contrast, the dynamic elastic moduli estimated using UPV on these same days are 25.10 GPa, 36.48 GPa, and 40.83 GPa, with corresponding relative errors of 71.9 %, 36.4 %, and 3.8 %. Overall, DWI-based elastic modulus estimations are consistently more accurate relative to the static values from compression tests compared to UPV-based estimations. However, the discrepancy between DWI-based and compression test moduli remains considerable before day seven. This discrepancy may be attributed to two factors:

- The relatively low elastic modulus in the early stage invalidates the linear approximation in Section 2.4.
- The S-wave velocity change during hydration is not accounted for. According to [19], the S-wave velocity plays a pivotal role in determining the early elastic modulus before 36 hours and cannot be disregarded.

To further quantify the accuracy of the constructed static elastic modulus, its evolution is used as input to calculate the stress evolution in the TSTM and ADTM tests, using a well-established finite element model for modelling the early-age stress evolution in concrete. The model uses classical Kelvin or Maxwell rheological chains to capture the aging viscoelastic properties of early-age concrete from the setting time. The evolution of induced strain or stress under the conditions of creep and relaxation is calculated in an incremental quasi-elastic manner utilizing exponential algorithms [72]. Appendix A presents the general theoretical basis and procedures for implementing the model to calculate stress evolution with different elastic moduli as input. For more details, refer to the authors' previous work [56,73–75].

Fig. 18 showcases the predicted stress evolution using the developed model with elastic modulus values obtained from UPV, DWI, and mechanical tests. To ensure consistency in the number of data points, we used one data point per hour by employing spline interpolation with different elastic moduli. The root mean square error (RMSE) evaluated the performance of different elastic moduli in stress prediction, with the results outlined in Table 5. In contrast to the estimation based on the dynamic elastic modulus acquired using UPV, the DWI-based estimation offers a more accurate prediction of stress evolution. This demonstrates that the proposed DWI-based ultrasonic approach provides a more precise estimation of static elastic modulus than conventional UPV-based ultrasonic approach. Discrepancies between DWI-based and compression test-based estimations before 168 hours (7 days) can be attributed to the reasons discussed earlier.

5. Discussion

5.1. Suggestions for applying the proposed approach

In this section, we will offer suggestions for future applications of the proposed approach, focusing on ultrasonic sensor selection and its potential use in concrete infrastructure. It is important to note that this approach cannot completely replace mechanical compression testing for determining the static elastic modulus. However, it serves as a valuable complement for monitoring changes in the static elastic modulus within existing structures, where multiple mechanical compression tests are less feasible.

5.1.1. Requirements for mixtures and ultrasonic sensors

We expect the proposed approach to achieve reasonable accuracy in

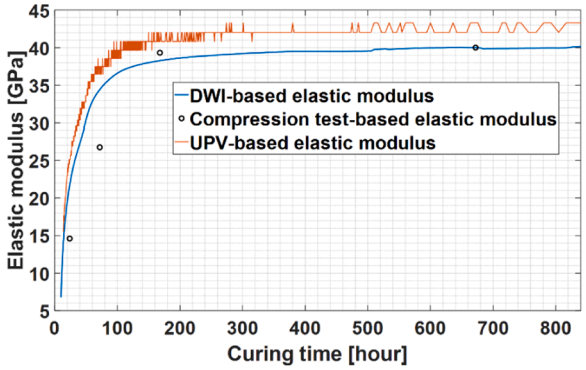

Fig. 17. Comparison between DWI-based elasticity modulus, UPV-based elasticity modulus and prism compression test-based elastic modulus.

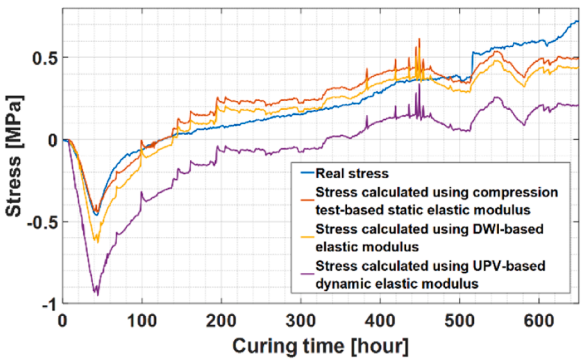

Fig. 18. Predicted stress evolution using the model with elastic moduli from UPV, DWI and compression test.

Table 5
RMSE of different methods with respect to the real stress.

		Static elastic modulus E_c		Dynamic elastic modulus E_d
		Compression test	DWI	UPV
RMSE [MPa]	From 0 hour	0.0965	0.1069	0.3010
	From 168 hours	0.1080	0.1081	0.2816

predicting the static elastic modulus when it exceeds 30 GPa, where the relationship between dynamic and static moduli approximates linearity. Additionally, the density and dynamic Poisson's ratio remain relatively constant at this range. However, if the static elastic modulus significantly deviates from its 28-day value, such as by 10 GPa as discussed in Section 2.4, the maximum error between the actual and estimated static elastic modulus could be up to 10 %. This approach is expected to be applicable to different mixtures, provided that the relationship between dynamic and static moduli remains linear beyond 30 GPa.

Since the proposed approach relies on stretching techniques and ballistic longitudinal waves, it is unsuitable for processing surface (Rayleigh) waves due to their different velocity expressions. The velocity change retrieved using the stretching technique is a relative measurement, theoretically unaffected by the distance between sender and receiver. Additionally, due to the use of ballistic waves, the approach is not sensitive to specimen geometry, as the wave trajectory is a straight line from sender to receiver. A potential variable that might affect the retrieved velocity change is the spatial variation of mechanical properties in concrete [76], which suggests that measurements from sensor pairs in different locations may yield slightly different results. Therefore, the stretching technique should not be applied to measurements from different sensor pairs.

Longitudinal waves can be generated using either surface-bonded or embeddable ultrasonic sensors. For surface-bonded sensors, it is crucial to ensure the received waves are comparable in waveform similarity to ensure reliable velocity change measurements [51], necessitating consistent sensor locations. Embeddable sensors might be a better option since they are embedded in concrete infrastructures, maintaining their locations throughout the service life of the structure. Furthermore, the usage of embeddable ultrasonic sensors can also facilitate the application of the stretching technique, since this technique requires less environmental variation and strong coupling. Moreover, these sensors, combined with an appropriate monitoring system, enable real-time and in-situ monitoring of concrete infrastructures [77,78].

5.1.2. Potential applications

The proposed approach has two potential applications: tracking changes in the static elastic modulus during concrete hydration and monitoring the degradation of the static elastic modulus due to freeze-thaw cycles and chemical attacks. In both cases, the static elastic modulus is estimated using relative velocity changes. Since this approach relies on relative velocity changes, it does not provide the absolute value of the static elastic modulus. To convert the relative values into absolute ones, a reference measurement is needed.

It is not necessary to perform mechanical tests simultaneously with each measurement; instead, only one mechanical test is required on a specific date. For tracking changes in the static elastic modulus during concrete hydration, it is recommended to use the static elastic modulus measured on the 28th day as the reference value. For monitoring degradation due to freeze-thaw cycles and chemical attacks, the reference should be the static elastic modulus of the concrete in a healthy state, before any damage-induced degradation occurs. Additionally, if there is significant temperature variation, dedicated temperature calibration is necessary for each measurement.

The proposed DWI-based ultrasonic approach also offers a potential in estimating the static elastic modulus in situ, with promising implications for integration with digital twins. Specifically, this approach could help to update the static elastic modulus within digital models, utilizing the modulus values estimated through this approach. As highlighted earlier, accurately tracking the static elastic modulus is crucial for precise structural calculations but poses challenges with existing non-destructive testing approaches. The proposed approach requires only a single input from a mechanical test, which simplifies its implementation compared to current approaches. Given the complexity and importance of maintaining accurate material properties in digital models, this approach represents an effective tool for enhancing the fidelity of structural simulations and ensuring that digital twins reflect real-world conditions more accurately.

We observed divergent behaviours in the development of P-wave and S-wave amplitudes between 54 hours and 96 hours, as depicted in Fig. 11(c). Specifically, the amplitude reaches a stable state in the P-wave or direct wave portion, while in the later part of the wave, which comprises both P-wave and S-wave but is dominated by the S-wave [40], the amplitude continues to grow. The rapid growth of wave energy before 50 hours is likely attributed to the evolution of the connected solid volume. As all solid phases become interconnected, the growth in P-wave energy slows down. Simultaneously, the connected solid phase significantly enhances the shear capacity of the concrete, which is manifested in the waves as a rapid increase in S-wave amplitude. This assertion can be verified by simultaneously tracking the velocities of both P-wave and S-wave using wave interferometry during hydration. In our future work, we will explore the physical correlation between the hydration mechanism and wave energy, which is proportional to the square of the amplitude, by leveraging the diffusive properties of elastic waves in concrete. These properties, particularly diffusivity, can be used to quantify changes in the interfacial transition zone during hydration [79,80].

5.2. Effect of stress changes on retrieved velocity changes in TSTM test

As explained in Section 2.2, the concrete sample in the TSTM test is constrained in deformation. Consequently, the observed velocity change in this test consists of two components: one arising from the development of mechanical properties during concrete hydration and the other resulting from the applied stress. The maximum stress reached in the final stage is approximately 0.8 MPa. Previous studies [36,81–85] have indicated that the velocity change induced by stress at this magnitude is around 1 ‰, which is considered negligible compared to the velocity change attributed to hydration.

5.3. Robustness of the proposed method

The robustness of the proposed method is not examined in this paper. We anticipate that two factors may influence its performance: the spatial variation of mechanical properties in concrete [76] and temperature fluctuations [48]. The first factor is an inherent characteristic of concrete, indicating that the static elastic modulus may vary spatially within the material. This can be addressed by using multiple sensors arranged in a grid to estimate the static elastic modulus across a given area. The second factor involves the impact of temperature on the velocity of longitudinal waves in concrete. To counteract this effect, dedicated temperature calibration is required for each measurement, i.e., the approach adopted by Zhang et al. [86].

5.4. Further investigation on the relationship between static and dynamic elastic moduli

This paper mentioned two influential factors that impact the relationship between static and dynamic elastic moduli in concrete: microplastic-related strain amplitude and viscoelasticity-related strain rate. While the ultrasonic approaches can mitigate the influence of strain

amplitude, the frequency effect remains present and cannot be completely eliminated. Research has been conducted on sedimentary rocks to gain a better understanding of this mechanism [52]. An interesting conclusion proposed by Tutuncu et al. [52] is that: *the strain amplitude-dependence is at least as significant as the viscoelastic effects*. In the case of concrete, the pronounced heterogeneity further amplifies the role played by strain amplitude in this process. The current relationships between static and dynamic elastic modulus are primarily empirical and are only applicable within a limited range. Quantifying the effects of viscoelasticity and microplasticity in measuring elastic modulus will aid in formulating a more comprehensive semi-empirical formula that can describe this relationship more universally.

6. Conclusion

This paper demonstrates a signal processing technique for estimating the static elastic modulus during concrete hydration. In contrast to conventional approaches that directly derive the dynamic elastic modulus from absolute velocity measurements, the proposed approach utilizes velocity changes obtained from DWI to track the evolution of the relative elastic modulus. By incorporating one input value from the static elastic modulus measured through the compression test, the elastic modulus evolution can be constructed. The experimental results indicate that the elastic modulus derived from the newly proposed DWI-based ultrasonic approach consistently provides more accurate estimates of the static elastic modulus compared to the UPV-based dynamic elastic modulus. The relative errors between the DWI-based and compression test-based elastic moduli on days one, three, and seven are 49.1 %, 28.7 %, and 2.6 %, respectively. In comparison, the relative errors between the UPV-based and compression test-based elastic moduli are 71.9 %, 36.4 %, and 3.8 %. To further validate the accuracy of the estimated static elastic modulus, this modulus, along with the static elastic modulus measured through prism compression test and the UPV-based dynamic elastic modulus, are input into a stress evolution model to predict the shrinkage-induced stress during concrete hydration. The model output demonstrates that the stress evolution predicted using the DWI-based elastic modulus, with an RMSE of 0.1069 MPa relative to actual values, is comparable to that predicted using the compression test-based static elastic modulus, which has an RMSE of 0.0965 MPa. In contrast, the RMSE of stress evolution predicted using the UPV-based dynamic elastic modulus is 0.3010 MPa, significantly higher than that of the DWI-based elastic modulus. The differences between the predictions based on the static and estimated elastic moduli before seven days can be attributed to the inapplicability of the linearity assumption between static and dynamic elastic moduli during the early stage characterized by low magnitude of elastic modulus.

CRediT authorship contribution statement

Hao Cheng: Writing – review & editing, Writing – original draft, Software, Methodology, Investigation, Formal analysis, Data curation, Conceptualization. **Minfei Liang:** Writing – review & editing, Writing – original draft, Methodology, Investigation, Conceptualization.

Declaration of Competing Interest

The authors declare that they have no known competing financial interests or personal relationships that could have appeared to influence the work reported in this paper.

Appendix A. Modelling the early-age stress evolution of concrete induced by autogenous shrinkage

The model of early-age stress evolution generally requires three types of inputs [56]: autogenous deformation, creep, and elastic modulus. In this paper, autogenous deformation and creep are obtained from the ADTM test and Bayesian inverse modeling methods [73], respectively. Combining these with the elastic modulus derived from compressive test-based, DWI-based, and UPV-based methods allows for the prediction of stress evolution, which can then be compared with the actual stress evolution measured by the TSTM test. This comparison helps evaluate the effectiveness of different methods for calculating the elastic modulus. The theoretical basis and modeling procedures are briefly introduced as follows.

Assuming early-age concrete follows a linear viscoelastic constitutive relationship, its early-age viscoelasticity can be characterized by the following Volterra integral:

$$\varepsilon(t) = \int_0^t J(t,t')\,\mathrm{d}\sigma(t') \quad , \tag{A1}$$

where ε denotes the strain, J is the creep compliance function, t is the age of concrete, and t' is the age when loads are applied. Rearranging the Volterra integral into its incremental form and assuming a linear variation of stress at each time step, the quasi-elastic constitutive relationship can be obtained:

$$\Delta\sigma = E^*\Delta\varepsilon - \sigma^* \quad , \tag{A2a}$$

$$E^* = \frac{\Delta t}{\int_{t_i}^{t_{i+1}} J(t_{i+1},t')\,\mathrm{d}t'} \quad , \tag{A2b}$$

$$\sigma^* = E^* \int_0^{t_i} [J(t_{i+1},t') - J(t_i,t')]\dot{\sigma}\,\mathrm{d}t' \quad , \tag{A2c}$$

where Δt denotes the time interval between two consecutive time steps t_i and t_{i+1}; $\Delta\sigma$ and $\Delta\varepsilon$ are difference of stress and strain between these two time steps. Note that the integration in Eq. (A2c) requires revisiting the entire load history, which makes FEM modeling very difficult. To address this, the rate-type creep law and exponential algorithm [72] were developed to convert the integral into a series of linear differential equations, which form the governing equations of the Kelvin or Maxwell rheological chains. In this model, the Kelvin chain is used, with its creep compliance represented as a Dirichlet series, as shown below:

$$J(t,t') = \frac{1}{E_0(t')} + \sum_{j=1}^{N} \frac{1}{E_j(t')}\left(1 - e^{-\frac{t-t'}{\mu_j}}\right) \quad , \tag{A3}$$

where N is the number of Kelvin chain units; E_j and μ_j is the elastic modulus and retardation time of j-th Kelvin chain units. To quantify concrete creep, this paper uses the following ACI-based equation [87]:

$$J(t,t') = \frac{1}{E(t')} + C_0 C_1(t') C_2(\xi) \quad , \tag{A4}$$

where C_0 is a coefficient related to general concrete properties and environmental conditions; C_1 is a power function describing the aging of creep compliance, which depends only on the age of loading t'; C_2 is a power function representing the non-aging term, which depends only on the duration of loading ξ ($\xi = t\text{-}t'$). In this paper, C_0 and C_2 are calculated according to the ACI code [87], while C_1 is a modified term computed based on Bayesian inverse modelling as proposed in [73], using the results of TSTM and ADTM tests as inputs.

To obtain the Kelvin chain units, Eq. (A3) is fitted with the creep compliance J calculated from Eq. (A4). This paper uses 13 Kelvin units and selects the retardation time of each unit as a priori to avoid an ill-conditioned equation system [88], as shown below:

$$\mu_j = 10^{-6+j}, j = 1:13 \quad . \tag{A5}$$

The continuous form of the non-aging term in Eq. (A4) is expressed as follows:

$$C_2(\xi) = \int_0^{\infty} \frac{1 - e^{-\frac{\xi}{\mu_j}}}{E_j} \, \mathrm{d}\left(\ln \mu_j\right) \quad . \tag{A6}$$

Leveraging Widder's formula, the elastic modulus of each Kelvin chain unit can be calculated [88,89]:

$$\frac{1}{E_j} = -\ln 10 \times \lim_{k\to\infty} \frac{(-k\mu)^k}{(k-1)!} C_2^{(k)}(k\mu) \quad , \tag{A7}$$

where the spectrum of the third order (k=3) is used. By substituting Eq. (A3) into Eq. (A2b) and Eq. (A2c), and calculating the integral using the midpoint rule, the expressions for E^* and σ^* can be obtained by:

$$E^*(t^*) = \frac{1}{\frac{1}{E_0(t^*)} + \sum_{j=1}^{N} \frac{1}{E_j(t^*)} \left[1 - \left(1 - e^{-\frac{\Delta t}{\mu_j}}\right) \frac{\mu_j}{\Delta t}\right]} \quad , \tag{A8a}$$

$$\sigma^*(t_i) = E^*(t^*) \sum_{j=1}^{N} \left(1 - e^{-\frac{\Delta t}{\mu_j}}\right) \varepsilon_j^*(t_i) \quad , \tag{A8b}$$

$$\varepsilon_j^*(t_i) = \int_0^{t_i} \frac{\dot{\sigma}}{E_j(t')} e^{-\frac{t_i - t'}{\mu_j}} \, \mathrm{d}t' \quad , \tag{A8c}$$

$$\varepsilon_j^*(t_{i+1}) = e^{-\frac{\Delta t}{\mu_j}} \varepsilon_j^*(t_i) + \frac{1 - e^{-\frac{\Delta t}{\mu_j}}}{E^*(t_i)} \frac{\mu_j}{\Delta t} \Delta\sigma \quad , \tag{A8d}$$

where t^* represents the average of two consecutive time steps, t_i and t_{i+1}. Eq. (A2a) and Equation (A8) encompass the incremental viscoelastic constitutive relationship for simulating the stress evolution induced by autogenous deformation. Note that ε^* for each Kelvin chain unit is an internal state variable—a second-order strain tensor—that must be updated at each integration point according to Eq. (A8d) at every time step.

In commercial FEM software COMSOL Multiphysics, the material subroutine described by Eq. (A2a) and Equation (A8) is implemented to simulate the relaxation behavior observed in the TSTM test. A meshed dog-bone-shaped specimen is created (Figure A1(a)), with roller boundaries applied to the highlighted purple surfaces (Figure A1(b)). Considering autogenous deformation as isotropic in all directions, the quasi-elastic constitutive equation described by Eq. (A2a) is modified as follows:

$$\Delta\sigma = E^*(\Delta\varepsilon - \Delta\varepsilon_{\mathrm{ad}}) - \sigma^* \quad , \tag{A9}$$

where $\Delta\varepsilon_{\mathrm{ad}}$ is the autogenous strain occurring in each time interval, as tested by ADTM, and σ^* is the state variable that stores previous load histories and should be updated at each time step according to Equation (A8). Finally, the stress contour (Figure A1(c)) can be obtained, and the final stress is calculated by normalizing the normal stress along the x-axis across the cross-sectional area, expressed as follows:

$$\sigma_{\mathrm{M}}(t) = \frac{\iint \sigma_{xx} \, \mathrm{d}y\mathrm{d}z}{A} \quad , \tag{A10}$$

where σ_{xx} is the normal stress along the x-axis (i.e., the axial direction of dog-bone specimen), and A is the cross-sectional area of the y-z plane at $x = 0$.

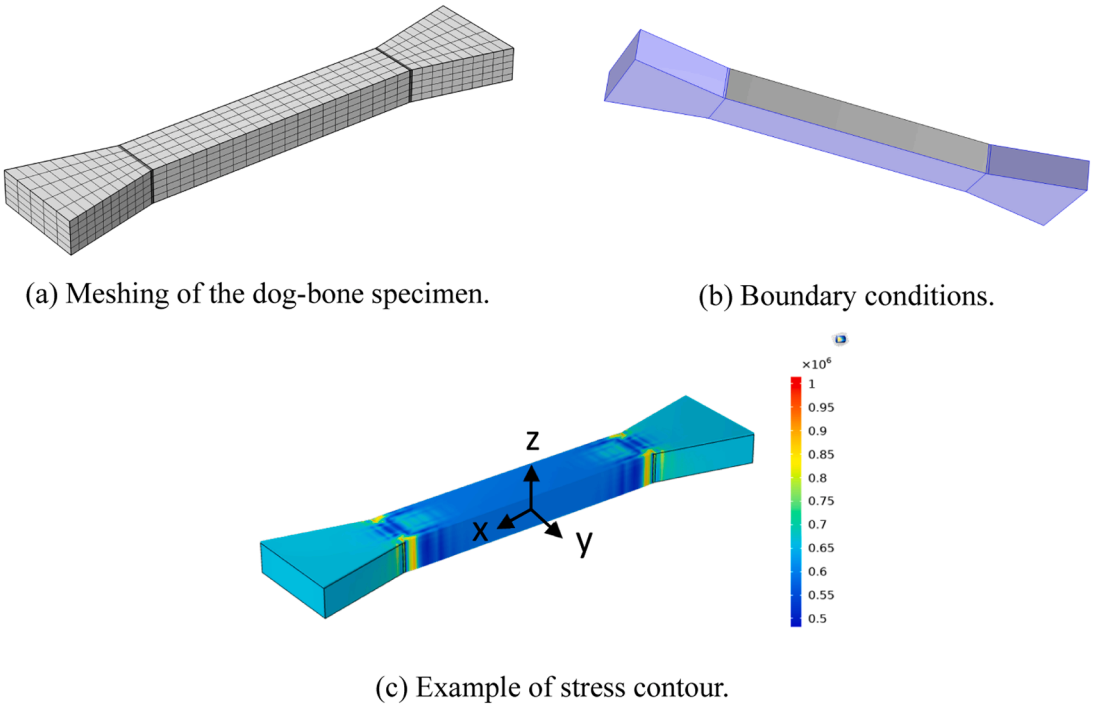

Figure A1. Numerical simulation of dog-bone specimen in COMSOL [73].

Appendix B. Mixture compositions involved in studies reported in Table 3

Mixture compositions involved in studies reported by Lyndon & Baladran [33], Mesbah, Lachemi & Aitcin [34], and Han & Kim [15] are provided in this appendix. Please note that the following tables are reproduced based on the mixture compositions provided in the respective articles.

Table B1
Mixture composition as reported by Lyndon & Baladran [33], reproduced from Table 3.1 in their article.

Mix	1	2	3
Cement-sand ratio	1:1; 1:2	1:1; 1:2	1:1; 1:2
Water-cement ratio	0.33; 0.39	0.33; 0.39	0.33; 0.39
Plastic concrete density [kg/m^3]	1950–2080	2015–2100	2400–2510
Cement quantity [kg/m^3]	340–680	340–680	340–680
Coarse aggregate volume fraction	0.5; 0.4; 0.3	0.5; 0.4; 0.3	0.5; 0.4; 0.3

Table B2
Mixture composition as reported by Mesbah, Lachemi & Aitcin [34], reproduced from Table 1 in their article. Please note that the cement involved in the mix type 1 is different from that involved in mix types 2 and 3.

Mix	1	2	3
Water-cement ratio	0.45	0.35	0.30
Water quantity [kg/m^3]	167	147	131
Cement quantity [kg/m^3]	372	420	450
Sand quantity [kg/m^3]	737	734	720
Gravel quantity [kg/m^3]	990	1030	1050
High-range water-reducing admixture [L/m^3]	0	5	7.4
Water-reducing agent [ml/m^3]	930	250	250
Air-entrained admixture [ml/m^3]	93	60	60

Table B3
Mixture composition as reported by Han & Kim [15], reproduced from Table 4 in their article. Please note that each mix type involves two different types of cement.

Mix	1	2
Water-cement ratio	0.40	0.50
Sand-aggregate ratio	0.39	0.42
Water quantity [kg/m^3]	181	181
Cement quantity [kg/m^3]	452	362
Sand quantity [kg/m^3]	630	707
Gravel quantity [kg/m^3]	989	989
Superplasticizer [cement × %]	0.5	0.5
Air-entrained admixture [cement × %]	0.005	0.005

Data Availability

Data will be made available on request.

References

[1] G. Ye, Experimental study and numerical simulation of the development of the microstructure and permeability of cementitious materials (Doctoral dissertation), Delft University of Technology, (2003). ISBN: 90-407-2435-0.
[2] P. Acker, F.J. Ulm, Creep and shrinkage of concrete: physical origins and practical measurements (DOI:), Nucl. Eng. Des. 203 (2001) 143–158, https://doi.org/10.1016/S0029-5493(00)00304-6.
[3] CEN (European Committee for Standardization), NEN-EN 12390-13: 2021 en: Testing hardened concrete - Part 13: Determination of secant modulus of elasticity in compression, CEN (European Committee for Standardization), (2021). Standards ICS codes: 91.100.30.
[4] American Society for Testing and Materials, ASTM C469-02: Standard test method for static modulus of elasticity and poisson's ratio of concrete in compression, American Society for Testing and Materials, (2017). DOI: 10.1520/C0469-02.
[5] E.I. Mashinsky, Differences between static and dynamic elastic moduli of rocks: Physical causes, Russ. Geol. Geophys. 44 (2003) 953–959.
[6] A.M. Neville, Properties of Concrete Vol. 4, Longman London, (1995). ISBN: 978-0-273-75580-7.
[7] H.M. Najm, O. Nanayakkara, M.M.S. Sabri, Destructive and non-destructive evaluation of fibre-reinforced concrete: a comprehensive study of mechanical properties (DOI:), Materials 15 (2022) 4432, https://doi.org/10.3390/ma15134432.
[8] C.A. Lara, J.F. De la Mora Gálvez, G. Cascante, M.D. Pandey, Static elastic modulus prediction at early ages using a modified resonant test for concrete cylinders using mems microphones, Case Stud. Constr. Mater. 20 (2024) e02864, https://doi.org/10.1016/j.cscm.2024.e02864.
[9] J.Y. Park, S.H. Sim, Y.G. Yoon, T.K. Oh, Prediction of static modulus and compressive strength of concrete from dynamic modulus associated with wave velocity and resonance frequency using machine learning techniques, Materials 13 (2020) 2886, https://doi.org/10.3390/ma13132886.
[10] J.L. Granja, M. Azenha, C. de Sousa, C. Ferreira, Comparison between different experimental techniques for stiffness monitoring of cement pastes, J. Adv. Concr. Technol. 12 (2014) 46–61, https://doi.org/10.3151/jact.12.46.
[11] Y. Zhou, J. Gao, Z. Sun, W. Qu, A fundamental study on compressive strength, static and dynamic elastic moduli of young concrete, Constr. Build. Mater. 98 (2015) 137–145, https://doi.org/10.1016/j.conbuildmat.2015.08.110.
[12] J. Silva, M. Azenha, A.G. Correia, C. Ferreira, Continuous stiffness assessment of cement-stabilised soils from early age, Géotechnique 63 (2013) 1419–1432, https://doi.org/10.1680/geot.13.P.021.
[13] M. Velay-Lizancos, I. Martinez-Lage, M. Azenha, J. Granja, P. Vazquez-Burgo, Concrete with fine and coarse recycled aggregates: E-modulus evolution, compressive strength and non-destructive testing at early ages, Constr. Build. Mater. 193 (2018) 323–331, https://doi.org/10.1016/j.conbuildmat.2018.10.209.
[14] C.F. Dunant, J. Granja, A. Muller, M. Azenha, K.L. Scrivener, Microstructural simulation and measurement of elastic modulus evolution of hydrating cement pastes, Cem. Concr. Res. 130 (2020) 106007, https://doi.org/10.1016/j.cemconres.2020.106007.
[15] S.H. Han, J.K. Kim, Effect of temperature and age on the relationship between dynamic and static elastic modulus of concrete, Cem. Concr. Res. 34 (2004) 1219–1227, https://doi.org/10.1016/j.cemconres.2003.12.011.
[16] G. Villain, L. Le Marrec, L. Rakotomanana, Determination of the bulk elastic moduli of various concretes by resonance frequency analysis of slabs submitted to impact echo, Eur. J. Environ. Civ. Eng. 15 (2011) 601–617, https://doi.org/10.3166/EJECE.15.601-617.
[17] American Society for Testing and Materials, ASTM C215-14: Standard test method for fundamental transverse, longitudinal and torsional resonant, frequencies of concrete specimens, American Society for Testing and Materials, 2020, https://doi.org/10.1520/C0215-14.
[18] V.G. Haach, L.M. Juliani, M.R.Da Roz, Ultrasonic evaluation of mechanical properties of concretes produced with high early strength cement, Constr. Build. Mater. 96 (2015) 1–10, https://doi.org/10.1016/j.conbuildmat.2015.07.139.
[19] J. Carette, C. Dumoulin, G. Karaiskos, S. Staquet, A. Deraemaeker, Monitoring of the E-modulus in early age concrete since setting time with embedded piezoelectric transducers, Proc. Struct. Faults + Repair, 14th Int. Conf. Exhib. (2012).
[20] G. Barluenga, J. Puentes, I. Palomar, C. Guardia, Methodology for monitoring Cement Based Materials at Early Age combining NDT techniques, Constr. Build. Mater. 193 (2018) 373–383, https://doi.org/10.1016/j.conbuildmat.2018.10.205.
[21] Y.Y. Lim, K.Z. Kwong, W.Y.H. Liew, C.K. Soh, Non-destructive concrete strength evaluation using smart piezoelectric transducer-a comparative study, Smart Mater. Struct. 25 (8) (2016), https://doi.org/10.1088/0964-1726/25/8/085021.
[22] G. Ionaşcu, A. Sandu, E. Manea, R. Gavrila, C. Comeaga, L. Bogatu, D. Besnea, Influence of geometry and material properties on resonant frequencies and sensitivity of MEMS cantilever-type structures, J. Optoelectron. Adv. Mater. 16 (2014) 579–590.
[23] H. Gu, G. Song, H. Dhonde, Y.L. Mo, S. Yan, Concrete early-age strength monitoring using embedded piezoelectric transducers, Smart Mater. Struct. 15 (2006) 1837–1845, https://doi.org/10.1088/0964-1726/15/6/038.
[24] G. Song, H. Gu, Y.L. Mo, T.T.C. Hsu, H. Dhonde, Concrete structural health monitoring using embedded piezoceramic transducers, Smart Mater. Struct. 16 (2007) 959–968, https://doi.org/10.1088/0964-1726/16/4/003.
[25] G. Song, H. Gu, Y.L. Mo, Smart aggregates: multi-functional sensors for concrete structures - a tutorial and a review, Smart Mater. Struct. 17 (2008) 033001, https://doi.org/10.1088/0964-1726/17/3/033001.
[26] G. Karaiskos, A. Deraemaeker, D.G. Aggelis, D. van Hemelrijck, Monitoring of concrete structures using the ultrasonic pulse velocity method (DOI:), Smart Mater. Struct. 24 (2015) 113001, https://doi.org/10.1088/0964-1726/24/11/113001.
[27] A.H. Mahmood, M. Babaee, S.J. Foster, A. Castel, Capturing the early-age physicochemical transformations of alkali-activated fly ash and slag using ultrasonic pulse velocity technique, Cem. Concr. Compos. 130 (2022) 104529, https://doi.org/10.1016/j.cemconcomp.2022.104529.
[28] R. Jones, The non-destructive testing of concrete, Mag. Concr. Res. 1 (1949) 67–78, https://doi.org/10.1680/macr.1949.1.2.67.
[29] J. Krautkrämer, H. Krautkrämer, Ultrasonic testing of materials, Springer Science & Business Media, 2013. ISBN: 978-3-662-10682-2.
[30] L.D. Landau, E.M. Lifshitz. Theory of elasticity: Volume 7, Elsevier, (1986). ISBN: 0-7506-2633-X.
[31] P. Wiciak, G. Cascante, M.A. Polak, Frequency and geometry effects on ultrasonic pulse velocity measurements of concrete specimens, Acids Mater. J. 117 (2020) 205–216, https://doi.org/10.14359/51722399.
[32] British Standard Institution, BS 8110: Structural Use of Concrete - Part 2. Code of Practice for Special Circumstances, British Standard Institution, London, (1985). Standards ICS codes: 91.080.40.
[33] F. Lydon, R. Balendran, Some observations on elastic properties of plain concrete (DOI:), Cem. Concr. Res. 16 (1986) 314–324, https://doi.org/10.1016/0008-8846(86)90106-7.
[34] H.A. Mesbah, M. Lachemi, P.-C. Aitcin, Determination of elastic properties of high-performance concrete at early ages, DOI: Acids Mater. J. 99 (2002) 37–41, https://doi.org/10.14359/11314.
[35] S. Popovics, Verification of relationships between mechanical properties of concrete-like materials, Mat. ériaux Et. Constr. 8 (1975) 183–191, https://doi.org/10.1007/BF02475168.
[36] B. Zhong, J. Zhu, G. Morcous, Measuring acoustoelastic coefficients for stress evaluation in concrete (DOI:), Constr. Build. Mater. 309 (2021) 125127, https://doi.org/10.1016/j.conbuildmat.2021.125127.
[37] K. Aki, B. Chouet, Origin of coda waves: source, attenuation, and scattering effects, J. Geophys. Res. 80 (1975) 3322–3342, https://doi.org/10.1029/JB080i023p03322.
[38] A. Curtis, P. Gerstoft, H. Sato, R. Snieder, K. Wapenaar, Seismic interferometry—turning noise into signal, Lead. Edge 25 (2006) 1082–1092, https://doi.org/10.1190/1.2349814.
[39] R.L. Weaver, On diffuse waves in solid media (DOI:), J. Acoust. Soc. Am. 71 (1982) 1608–1609, https://doi.org/10.1121/1.387816.
[40] R. Snieder, Coda wave interferometry and the equilibration of energy in elastic media, Phys. Rev. E 66 (2002) 046615, https://doi.org/10.1103/PhysRevE.66.046615.
[41] F. Zhu, T. Zhao, T. Guan, Influence of water content on dynamic elastic modulus of concrete, Appl. Mech. Mater. (2013) 1605–1609, https://doi.org/10.4028/www.scientific.net/AMM.351-352.1605.

[42] M. Liang, Z. Chang, Y. Zhang, H. Cheng, S. He, E. Schlangen, B. Šavija, Autogenous deformation induced-stress evolution in high-volume GGBFS concrete: Macro-scale behavior and micro-scale origin (DOI:), Constr. Build. Mater. 370 (2023) 130663, https://doi.org/10.1016/j.conbuildmat.2023.130663.
[43] CEN (European Committee for Standardization), NEN-EN 12390-3: 2019 en: Testing hardened concrete - Part 3: Compressive strength of test specimens, CEN (European Committee for Standardization), (2019). Standards ICS codes: 91.100.30.
[44] N. Maeda, A method for reading and checking phase times in autoprocessing system of seismic wave data (DOI:), Zisin 38 (1985) 365–379, https://doi.org/10.4294/ZISIN1948.38.3_365.
[45] H. Reinhardt, C. Grosse, Continuous monitoring of setting and hardening of mortar and concrete, Constr. Build. Mater. 18 (2004) 145–154, https://doi.org/10.1016/j.conbuildmat.2003.10.002.
[46] J.H. Kurz, C.U. Grosse, H.-W. Reinhardt, Strategies for reliable automatic onset time picking of acoustic emissions and of ultrasound signals in concrete, Ultrasonics 43 (2005) 538–546, https://doi.org/10.1016/j.ultras.2004.12.005.
[47] H. Zhang, C. Thurber, C. Rowe, Automatic P-wave arrival detection and picking with multiscale wavelet analysis for single-component recordings, Bull. Seismol. Soc. Am. 93 (2003) 1904–1912, https://doi.org/10.1785/0120020241.
[48] R. Snieder, A. Gret, H. Douma, J. Scales, Coda wave interferometry for estimating nonlinear behavior in seismic velocity, Science 295 (2002) 2253–2255, https://doi.org/10.1126/science.1070015.
[49] C. Sens-Schönfelder, U. Wegler, Passive image interferometry and seasonal variations of seismic velocities at Merapi Volcano, Indonesia, L21302. DOI: Geophys. Res. Lett. 33 (2006) https://doi.org/10.1029/2006GL027797.
[50] T. Planès, E. Larose, A review of ultrasonic Coda Wave Interferometry in concrete (DOI:), Cem. Concr. Res. 53 (2013) 248–255, https://doi.org/10.1016/j.cemconres.2013.07.009.
[51] H. Cheng, C. Weemstra, M.A.N. Hendriks, Y. Yang, Comparing the stretching technique and the wavelet cross-spectrum technique for measuring stress-induced wave-velocity changes in concrete, Autom. Constr. 158 (2024) 105221, https://doi.org/10.1016/j.autcon.2023.105221.
[52] A.N. Tutuncu, A.L. Podio, A.R. Gregory, M.M. Sharma, Nonlinear viscoelastic behavior of sedimentary rocks, Part I: Effect of frequency and strain amplitude (DOI:), Geophysics 63 (1998) 184–194, https://doi.org/10.1190/1.1444311.
[53] W. de Araujo Thomaz, D.Y. Miyaji, E. Possan, Comparative study of dynamic and static Young's modulus of concrete containing basaltic aggregates, Case Stud. Constr. Mater. 15 (2021) e00645, https://doi.org/10.1016/j.cscm.2021.e00645.
[54] K.K. Sideris, P. Manita, K. Sideris, Estimation of ultimate modulus of elasticity and Poisson ratio of normal concrete, Cem. Concr. Compos. 26 (2004) 623–631, https://doi.org/10.1016/S0958-9465(03)00084-2.
[55] L. Yu, J. Chen, H. Song, Experimental and theoretical analyses on the density and modulus development of concrete under continued hydration, Acta Mech. Solid. Sin. 31 (2018) 161–173, https://doi.org/10.1007/s10338-018-0019-5.
[56] M. Liang, J. Xie, S. He, Y. Chen, E. Schlangen, B. Šavija, Autogenous deformation-induced stress evolution in cementitious materials considering viscoelastic properties: A review of experiments and models, Dev. Built Environ. (2024) 100356, https://doi.org/10.1016/j.dibe.2024.100356.
[57] Q. Kong, Innovation in piezoceramic based structural health monitoring (Doctoral dissertation), University of Houston, (2015).
[58] S.W. Shin, C.B. Yun, J.S. Popovics, J.H. Kim, Improved Rayleigh wave velocity measurement for nondestructive early-age concrete monitoring, Res. Nondestruct. Eval. 18 (2007) 45–68, https://doi.org/10.1080/09349840601128762.
[59] V. Giurgiutiu, J. Bao, W. Zhao, Active sensor wave propagation health monitoring of beam and plate structures, In Smart Structures and Materials 2001: Smart Structures and Integrated Systems, International Society for Optics and Photonics, 2001, pp. 234-245. DOI: 10.1117/12.436535.
[60] M.J. Povey, Ultrasonic techniques for fluids characterization, Elsevier, 1997. ISBN-13: 978-0-12-563730-5.
[61] Q. Kong, S. Hou, Q. Ji, Y.L. Mo, G. Song, Very early age concrete hydration characterization monitoring using piezoceramic based smart aggregates (DOI:), Smart Mater. Struct. 22 (2013) 085025, https://doi.org/10.1088/0964-1726/22/8/085025.
[62] C.M. Sayers, A. Dahlin, Propagation of ultrasound through hydrating cement pastes at early times, Adv. Cem. Based Mater. 1 (1993) 12–21, https://doi.org/10.1016/1065-7355(93)90004-8.
[63] C. Dumoulin, G. Karaiskos, J. Carette, S. Staquet, A. Deraemaeker, Monitoring of the ultrasonic P-wave velocity in early-age concrete with embedded piezoelectric transducers, Smart Mater. Struct. 21 (2012) 047001, https://doi.org/10.1088/0964-1726/21/4/047001.
[64] A. Boumiz, C. Vernet, F.C. Tenoudji, Mechanical properties of cement pastes and mortars at early ages: Evolution with time and degree of hydration (DOI:), Adv. Cem. Based Mater. 3 (1996) 94–106, https://doi.org/10.1016/S1065-7355(96)90042-5.
[65] C. Boulay, S. Staquet, M. Azenha, A. Deraemaeker, M. Crespini, J. Carette, J. Granja, B. Delsaute, A. Dumoulin, G. Karaiskos, Monitoring elastic properties of concrete since very early age by means of cyclic loadings, ultrasonic measurements, natural resonant frequency of componant frequency of composite beam (EMM-ARM) and with smart aggregates, In VIII International Conference on Fracture Mechanics of Concrete and Concrete Structures, Framcos, 8 (2013), 12p.
[66] G. Trtnik, M. Gams, Recent advances of ultrasonic testing of cement based materials at early ages (DOI:), Ultrasonics 54 (2014) 66–75, https://doi.org/10.1016/j.ultras.2013.07.010.
[67] J. Carette, S. Staquet, Monitoring the setting process of mortars by ultrasonic P and S-wave transmission velocity measurement, Constr. Build. Mater. 94 (2015) 196–208, https://doi.org/10.1016/j.conbuildmat.2015.06.054.
[68] X. Wang, J. Chakraborty, A. Bassil, E. Niederleithinger, Detection of Multiple Cracks in Four-Point Bending Tests Using the Coda Wave Interferometry Method (DOI:), Sensors 20 (2020) 1986, https://doi.org/10.3390/s20071986.
[69] H. Hu, D. Li, L. Wang, R. Chen, X. Xu, An improved ultrasonic coda wave method for concrete behavior monitoring under various loading conditions, Ultrasonics 116 (2021) 106498, https://doi.org/10.1016/j.ultras.2021.106498.
[70] M. Azenha, F. Magalhães, R. Faria, Á. Cunha, Measurement of concrete E-modulus evolution since casting: A novel method based on ambient vibration, Cem. Concr. Res. 40 (2010) 1096–1105, https://doi.org/10.1016/j.cemconres.2010.02.014.
[71] D.S. Hughes, J. Kelly, Second-order elastic deformation of solids, Phys. Rev. 92 (1953) 1145, https://doi.org/10.1103/PhysRev.92.1145.
[72] Z.P. Bažant, M. Jirásek, Creep and hygrothermal effects in concrete structures, Vol. 225, Springer, 2018.
[73] M. Liang, Z. Li, S. He, Z. Chang, Y. Gan, E. Schlangen, B. Šavija, Stress evolution in restrained GGBFS concrete due to autogenous deformation: bayesian optimization of aging creep, Constr. Build. Mater. 324 (2022) 126690, https://doi.org/10.1016/j.conbuildmat.2022.126690.
[74] M. Liang, Z. Chang, S. He, Y. Chen, Y. Gan, E. Schlangen, B. Šavija, Predicting early-age stress evolution in restrained concrete by thermo-chemo-mechanical model and active ensemble learning, Comput. -Aided Civ. Infrastruct. Eng. 37 (2022) 1809–1833, https://doi.org/10.1111/mice.12915.
[75] M. Liang, G.D. Luzio, E. Schlangen, B. Šavija, Experimentally informed modeling of the early-age stress evolution in cementitious materials using exponential conversion from creep to relaxation (DOI:), Comput. -Aided Civ. Infrastruct. Eng. (2024) 1–24, https://doi.org/10.1111/mice.13156.
[76] N.T. Nguyen, Z.M. Sbartaï, J.F. Lataste, D. Breysse, F. Bos, Assessing the spatial variability of concrete structures using NDT techniques–Laboratory tests and case study, Constr. Build. Mater. 49 (2013) 240–250, https://doi.org/10.1016/j.conbuildmat.2013.08.011.
[77] H. Cheng, F. Zhang, Y. Yang, C.B.M. Blom, Monitoring of repaired concrete floor in the Maastunnel using smart aggregates, In Bridge Maintenance, Safety, Management, Life-cycle Sustainability and Innovations, 2022, pp. 493-500. DOI: 10.1201/9781003322641-57.
[78] C. Dumoulin, A. Deraemaeker, All-season monitoring of concrete repair in an urban tunnel in Brussels using embedded ultrasonic transducers with emphasis on robustness to environmental variations, J. Civ. Struct. Health Monit. 11 (2021) 879–895, https://doi.org/10.1007/s13349-021-00486-9.
[79] M. Ramaniraka, S. Rakotonarivo, C. Payan, V. Garnier, Effect of the interfacial transition zone on ultrasonic wave attenuation and velocity in concrete, Cem. Concr. Res. 124 (2019) 105809, https://doi.org/10.1016/j.cemconres.2019.105809.
[80] M. Ramaniraka, S. Rakotonarivo, C. Payan, V. Garnier, Effect of interfacial transition zone on diffuse ultrasound in thermally damaged concrete (DOI:), Cem. Concr. Res. 152 (2022) 106680, https://doi.org/10.1016/j.cemconres.2021.106680.
[81] I. Lillamand, J.F. Chaix, M.A. Ploix, V. Garnier, Acoustoelastic effect in concrete material under uni-axial compressive loading, NDT E Int. 43 (2010) 655–660, https://doi.org/10.1016/j.ndteint.2010.07.001.
[82] C.L. Nogueira, K.L. Rens, Acoustoelastic response of concrete under uniaxial compression, Acids Mater. J. 116 (2019) 21–33, https://doi.org/10.14359/51714462.
[83] E. Larose, S. Hall, Monitoring stress related velocity variation in concrete with a 2×10^{-5} relative resolution using diffuse ultrasound, J. Acoust. Soc. Am. 125 (2009) 1853–1856, https://doi.org/10.1121/1.3079771.
[84] D.P. Schurr, J.Y. Kim, K.G. Sabra, L.J. Jacobs, Damage detection in concrete using coda wave interferometry, NDT E Int. 44 (2011) 728–735, https://doi.org/10.1016/j.ndteint.2011.07.009.
[85] S.C. Stahler, C. Sens-Schonfelder, E. Niederleithinger, Monitoring stress changes in a concrete bridge with coda wave interferometry, J. Acoust. Soc. Am. 129 (2011) 1945–1952, https://doi.org/10.1121/1.3553226.
[86] Y. Zhang, O. Abraham, V. Tournat, A. Le Duff, B. Lascoup, A. Loukili, F. Grondin, O. Durand, Validation of a thermal bias control technique for Coda Wave Interferometry (CWI), Ultrasonics 53 (2013) 658–664, https://doi.org/10.1016/j.ultras.2012.08.003.
[87] C. Videla, D.J. Carreira, N. Garner, Guide for modeling and calculating shrinkage and creep in hardened concrete, ACI report, reported by ACI Committee 209.
[88] Z.P. Bažant, Y. Xi, Continuous retardation spectrum for solidification theory of concrete creep, J. Eng. Mech. 121 (1995) 281–288, https://doi.org/10.1061/(ASCE)0733-9399(1995)121:2(281).
[89] Z.P. Bažant, R. L'Hermite, Mathematical modeling of creep and shrinkage of concrete, 1988, 163.